THESIS

USING CONTINUOUS [CO_2] DATA IN INVERSE MODELS TO REDUCE UNCERTAINTY IN GLOBAL AND REGIONAL ESTIMATES OF CARBON FLUX

Submitted by

Joanne Skidmore

Department of Atmospheric Science

In partial fulfillment of the requirements

For the Degree of Master of Science

Colorado State University

Fort Collins, Colorado

Spring 2004

COLORADO STATE UNIVERSITY

December 15, 2003

WE HEREBY RECOMMEND THAT THE THESIS PREPARED UNDER OUR SUPERVISION BY JOANNE SKIDMORE ENTITLED "USING CONTINUOUS [CO_2] DATA IN INVERSE MODELS TO REDUCE UNCERTAINTY IN GLOBAL AND REGIONAL ESTIMATES OF CARBON FLUX" BE ACCEPTED AS FULFILLING IN PART REQUIREMENTS FOR THE DEGREE OF MASTER OF SCIENCE.

Committee on Graduate Work

_____

_____

_____

_____

Advisor

_____

Department Head

ABSTRACT OF THESIS

USING CONTINUOUS [CO_2] DATA IN INVERSE MODELS TO REDUCE UNCERTAINTY IN GLOBAL AND REGIONAL ESTIMATES OF CARBON FLUX

The current atmospheric CO_2 concentration observing network is based on weekly flask samples from the atmosphere, most of which are taken in remote marine locations. These sites are used because the tropospheric air being sampled is well-mixed and isolated from influences of populated and vegetated areas and therefore sufficient to capture background concentrations. These networks however, are limited by the lack of measurements from continental sites and are therefore too sparse to monitor regional fluxes. The continental regions suffer most from lack of observations, due to difficulties in measuring where landscape heterogeneity, strong vertical gradients, and dynamic diurnal cycles persist. Measurements taken at tall tower sites try to avoid these difficulties by measuring in the mixed-layer, but they are very expensive to implement and maintain. Shorter flux towers take measurements in the canopy surface-layer, but the grid cells of global circulation models represent measurements from the higher mixed-layer. In order to harmonize real observations and theoretical models there must be reconciliation between these disparate representations. The measurements of shorter surface-layer flux towers would be reasonable to use if they could be extrapolated to represent mixed-layer CO_2 concentrations.

"Virtual" tall towers might be the answer to this problem as they can be constructed using measurements of calibrated CO_2 and fluxes from short towers, in a methodology that is currently being tested at a real tall tower in Wisconsin.

Previous studies in optimization of carbon observing networks considered any global grid cell as eligible for selection as a measurement site. In reality, measurement of mean CO_2 over highly variable terrestrial regions is very impractical and expensive. A global network of eddy-covariance flux towers already exists in which continuous measurements of CO_2 are taken, as well as measurements of sensible heat (H) and latent heat (LE), such that net ecosystem exchange (NEE) can be estimated. If the CO_2 measurements were calibrated, these surface layer values could be extrapolated to the mixed-layer using similarity theory providing a means to sample the continental mixed-layer for use in global inversions to further constrain the carbon budget. With this method for estimating the mid-day continental boundary layer CO_2 from calibrated CO_2 and eddy-covariance measurements at flux towers, a network of virtual tall towers could be readily implemented using existing infrastructure and minimal additional instrumentation. This is potentially a reasonable solution to the problem of large underconstrained continental regions. The purpose of this study is to investigate to what degree incorporating precise virtual tall tower [CO_2] data into inversions of global transport models will reduce global and regional estimates of carbon fluxes, and to determine if this would further constrain the continental regions that currently persist as a problem to global optimization.

Using the Transcom3 experimental protocol, sites where high-frequency timeseries were saved from the forward runs of 12 transport models were used as eligible sites for possible global networks. The fluxes were optimized to fit the monthly mean of mid-day values by sub-sampling the global fields during the afternoon only, when this method works best.

I used a genetic algorithm optimization scheme to determine which existing measurement sites should be grouped together in a network that minimizes the root mean square uncertainty of carbon flux estimates. The algorithm produces the most "fit" network of flux tower sites by comparing and prioritizing them according to their performance in the inversions.

I performed a regional and global experiment to determine which configuration of five or ten towers, respectively, should be implemented first as virtual tall towers for the greatest uncertainty reduction. In the North American experiment, the optimal network selected five sites located in North Carolina, Kansas, Illinois, Tennessee, and Maryland. Overall, the strategies of bracketing the main flux areas and making observations through a gradient of fluxes didn't work well in the Transcom3 inversions. The best virtual tall tower networks emphasize placement of measuring sites *in* and just *downwind* of strong fluxes. In the global selection of ten towers, the algorithm selected four sites in North, Central, and South America in the strong flux areas of the tropics and eastern US. It selected two towers in southern Europe, even though Europe has a dense network, to constrain the regions of North and South Africa. Two towers were selected in Thailand

and two in Japan to constrain temperate and boreal Asia, respectively. In both experiments, using these optimal networks resulted in the most uncertainty reduction.

In another experiment, I tested the sensitivity of flux uncertainty reduction to representation error. The results show that adding five, ten and 24 virtual tall towers to the existing tall towers and flask sampling network reduced carbon flux estimate uncertainties in North America significantly by 25%, 50%, and 75%, respectively, as representation error is minimized to 2 ppm. This indicates that virtual tall towers can contribute meaningful information to regional and global inversions, thereby constraining continental regions and carbon budget estimates at minimal cost in a short amount of time.

Joanne Skidmore
Department of Atmospheric Science
Colorado State University
Fort Collins, CO 80523
Spring 2004

ACKNOWLEDGEMENTS

This project was supported under United States Department of Energy (DOE) Contract DE-FG03-02ER63474 A001.

Thank you to Professor Scott Denning, Kevin Gurney, and John Kleist for their dedicated technical and scientific support of this research. Thank you also to Professors Graeme Stephens and Indy Burke for their involvement in research development and assistance in technical writing.

TABLE OF CONTENTS

LIST OF TABLES

LIST OF FIGURES

CHAPTER 1. INTRODUCTION

1.1 Carbon in the Atmosphere

The current atmosphere is composed mostly of nitrogen and oxygen, in portions of 78% and 21%, respectively. In addition, there are trace amounts of water vapor, carbon dioxide, and ozone, which constitute less than 1% of the atmosphere's entire mass, that have significant influence over the Earth's climate due to their characteristics for absorption and emission of thermal infrared energy [*Wallace and Hobbs, 1977*]. The earth's surface temperature is observed to be higher than the effective earth temperature needed to balance the planet's radiation budget [*Hartmann, 1994*], and this is due to the presence of the atmosphere and these radiatively active minority constituents that make the surface of the planet warm enough to maintain life. Carbon dioxide contributes to this warming effect as a gas that is a weak absorber of visible light (shortwave) and a strong absorber of thermal infrared radiation (longwave). Its presence in the atmosphere implies that longwave radiation is being captured and re-emitted to the surface acting to insulate the planet. Because the surface is receiving more radiation from this layer, it compensates by emitting at a higher temperature and in this way the surface is warmer than it would be without an atmosphere. The climate is therefore sensitive to changes in the concentrations of these gases whether it be part of a natural cycle or induced by human activities.

During one annual cycle, approximately 120 Gigatons (Gt) of carbon (1 Gt C = 1 billion tons = 1 Pg C = 10^{15} g carbon) are exchanged between the atmosphere and the biosphere, while the ocean and atmosphere exchange ~ 90 Gt. As levels of CO_2 increase, questions have arisen concerning the relationship between greater concentrations of greenhouse gases in the atmosphere and changing global climate [*Tans, 1990*]. Changes in the atmosphere effect change in the entire earth system as there is coupling between the ocean, biosphere, and cryosphere. Climate variability is thought to be a response by these systems to changes in external forcing of incident radiation as well as a response from internal fluctuations that induce powerful feedback mechanisms [*Wallace and Hobbs, 1977*]. The interaction of these systems is complex and difficult to observe. Thus, the relationship between increasing CO_2 and global warming is not simple, unilateral, or obvious.

The Intergovernmental Panel on Climate Change (IPCC) was established by the United Nations in 1988 to serve as the scientific platform that informs the negotiations between countries on climate change and global warming. IPCC (2001) estimated that the average global temperature has increased by 1 degree Celsius over the last 100 years. They also concluded that the 1990s were the warmest decade, and that 1998 was the warmest year globally in the instrumental record that dates back to 1861. The average global surface temperature is calculated to be the average of near surface air temperature over land and sea, and has increased since 1861. During the 20th century, the IPCC estimates this increase to be 0.6 ± 0.2°C [*Houghton et al., 2001*]. Debate continues as to

whether this increase in temperature is due to rising levels of greenhouse gases in the atmosphere or part of a natural millennial-scale cycle.

1.2 Influence of Fossil Fuel Burning on Atmospheric Carbon

Fossil fuel begins as reduced organic matter that has accumulated very slowly in underground reservoirs for millions of years. It becomes oxidized during combustion and one of the many by-products that are formed, namely carbon dioxide (CO_2), remains as a stable substance in the atmosphere. Because this gas exists in trace amounts that are circulated without undergoing chemical reactions, it is commonly referred to as a "tracer".

Increasing emissions from fossil fuel burning, deforestation, cement manufacturing, and changes in land use have resulted in a ~ 30% increase in atmospheric concentrations of CO_2 since the 1870s [*IPCC, 2001*]. The level of CO_2 has risen from 280 ppmv (parts per million by volume of dry air) prior to the industrial revolution of the late 19^{th} century, to 367 ppmv in 1999 [*IPCC, 2001*]. This trend has been recorded at the Mauna Loa observatory in Hawaii since 1958, by the Scripps Institution for Oceanography (SIO) and the National Oceanic and Atmospheric Administration (NOAA). **Figure 1** shows the historical record from this site.

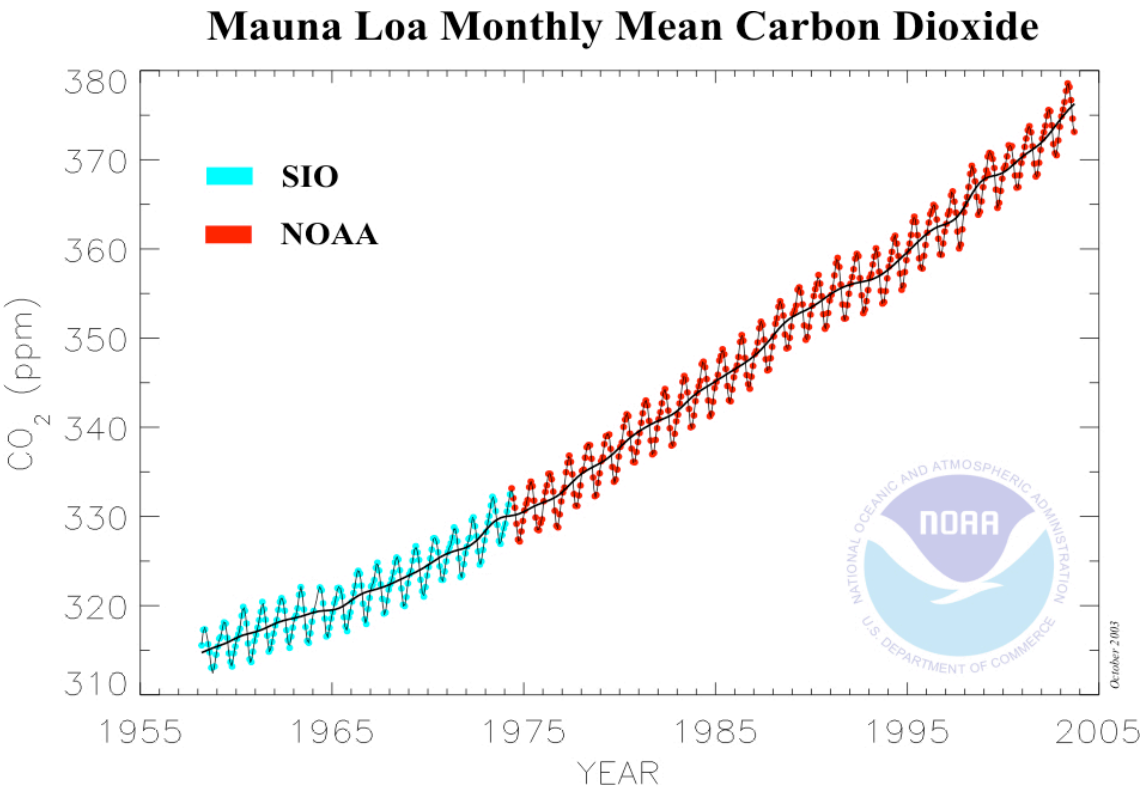

Atmospheric carbon dioxide monthly mean mixing ratios. Data prior to May 1974 are from the Scripps Institution of Oceanography (SIO, blue), data since May 1974 are from the National Oceanic and Atmospheric Administration (NOAA, red). A long-term trend curve is fitted to the monthly mean values. Principal investigators: Dr. Pieter Tans, NOAA CMDL Carbon Cycle Greenhouse Gases, Boulder, Colorado, (303) 497-6678, pieter.tans@noaa.gov, and Dr. Charles D. Keeling, SIO, La Jolla, California, (616) 534-6001, cdkeeling@ucsd.edu.

Figure 1. The historical CO_2 concentration record at the Mauna Loa observatory.

The record clearly indicates a seasonal variability in concentration corresponding to the annual northern hemispheric pattern of CO_2 uptake by photosynthesis during the growing season, and subsequent release in winter when more plants are dormant and soil microbial respiration exceeds photosynthetic uptake. The data record shows that a 17% increase in the mean annual concentration of CO_2 has occurred since 1959 [*Keeling et al., 2003*].

The history of atmospheric CO_2 is important because it can be used to discriminate between the biological or natural source and sink activity of the Earth's surface and the constructed anthropogenic emission rate. Carbon emissions from fossil fuel combustion are estimated by the Global Emissions Inventory Activity (GEIA) (*http://geiacenter.org*), a component of the International Atmospheric Chemistry Program (IGAC) of the International Geosphere-Biosphere Program (IGBP).

Approximately 6.3 Gt of carbon is introduced into the atmosphere every year due to fossil fuel burning and cement production [*Andres et al., 1996*]. Because energy consumption of developing countries is increasing and the fossil energy production of developed nations is expanding, it is assumed that these emissions will continue to be a source of carbon to the atmosphere in the coming decades [*CDIAC, 2003*]. Deforestation is estimated to be an additional source of ~ 1.6 Gt C yr^{-1} [*Schimel et al., 1995*]. Despite these perturbations, the rate of increase of CO_2 in the atmosphere is detected to be only half the amount that is being emitted each year by the primary source of fossil fuel burning [*Andres et al., 1996*]. The half being removed is taken up by the biosphere and dissolved into cold ocean waters [*Houghton et al., 2001*], while the remaining emissions are accumulating in the atmosphere as is evident in the Mauna Loa record. The terrestrial and oceanic sinks that currently account for the emissions uptake vary in strength every year, and it is difficult to determine their underlying mechanisms and how they will fluctuate in the future according to changes in the earth's climate [*Gruber et al., 1996*].

Fossil fuel carbon is released predominantly in the northern latitudes by industrial nations, and therefore a north-south gradient of 4 – 5 ppm should be evident in atmospheric CO_2 concentrations. The observed gradient of 3 ppm implies the existence of another "missing" source from the southern hemisphere, or sink in the northern hemisphere. *Tans et al.* [1990] suggested that it was most likely to be a carbon sink in boreal or temperate northern continents. More recent studies have cast confusion over the magnitude and location of this sink, such as the findings of *Fan et al.* [1998] which found that a 1.7 Gt C yr^{-1} terrestrial carbon sink in North America dominated the northern hemisphere between 1988-1992. In the next year, *Bousquet et al.* [1999] found the biggest sink of 1.5 Gt C yr^{-1} to be over Northern Asia and a weaker 0.5 Gt C yr^{-1} sink over North America. Studies of this sort regarding the natural source and sink activity of carbon, although sometimes contradictory, are imperative for investigating the earth's carbon budget and understanding future trends of global change.

1.3 Research Objective

In 1995 the United Nations' International Panel on Climate Change (IPCC) reported the annual "bottom-up" estimates of terrestrial sink processes and their uncertainties [*IPCC, 1995*]. The overall terrestrial sink is partitioned into four main processes that have been identified: forest regrowth, CO_2 fertilization, nitrogen fertilization, and climate fluctuations. The annual uptake estimates of each process are shown in **Table 1**.

Table 1. IPCC 1995 estimates of terrestrial carbon sink processes.

Process	Annual Uptake (Gt C yr^{-1})
Forest Regrowth	0.0 to 1.0
CO_2 Fertilization	0.5 to 2.0
Nitrogen Fertilization	0.2 to 1.0
Climate Fluctuations	0.0 to 1.0
Total	0.7 to 5.0

The net strength of these processes is estimated to be ~ 0.7 Gt C yr^{-1}, with an uncertainty that is greater by almost one order of magnitude. With such a large uncertainty, the total estimate value is not very useful.

The current atmospheric carbon budget is constrained by measurements of fluxes and concentrations. Flux measurements are local and act on very short timescales that vary in footprint and time making it difficult to assess a regional budget over a multi-year or multi-decadal period of time. These measurements are continually maintained by permanent infrastructure as well as field campaigns [*Baldocchi, 2003*].

The current CO_2 concentration observing network is based on weekly flask samples from the atmosphere, most of which are taken in remote marine locations. These sites are used because the tropospheric air being sampled is well-mixed and isolated from

influences of populated and vegetated areas and thus is sufficient to capture background concentrations. These networks however, are limited by the lack of measurements from continental sites and are therefore too sparse to monitor regional fluxes [*Masarie et al., 1995*]. This flask-sampling network of ~100 stations, as shown in **Figure 2**, is currently maintained by the Climate Monitoring Diagnostics Laboratory (CMDL) of the National Oceanic and Atmospheric Administration (NOAA) in Boulder, Colorado, and has been used to infer sources and sinks, e.g. *Bousquet et al., 2000* and *Gurney et al., 2002*, on continental and ocean-basin scales.

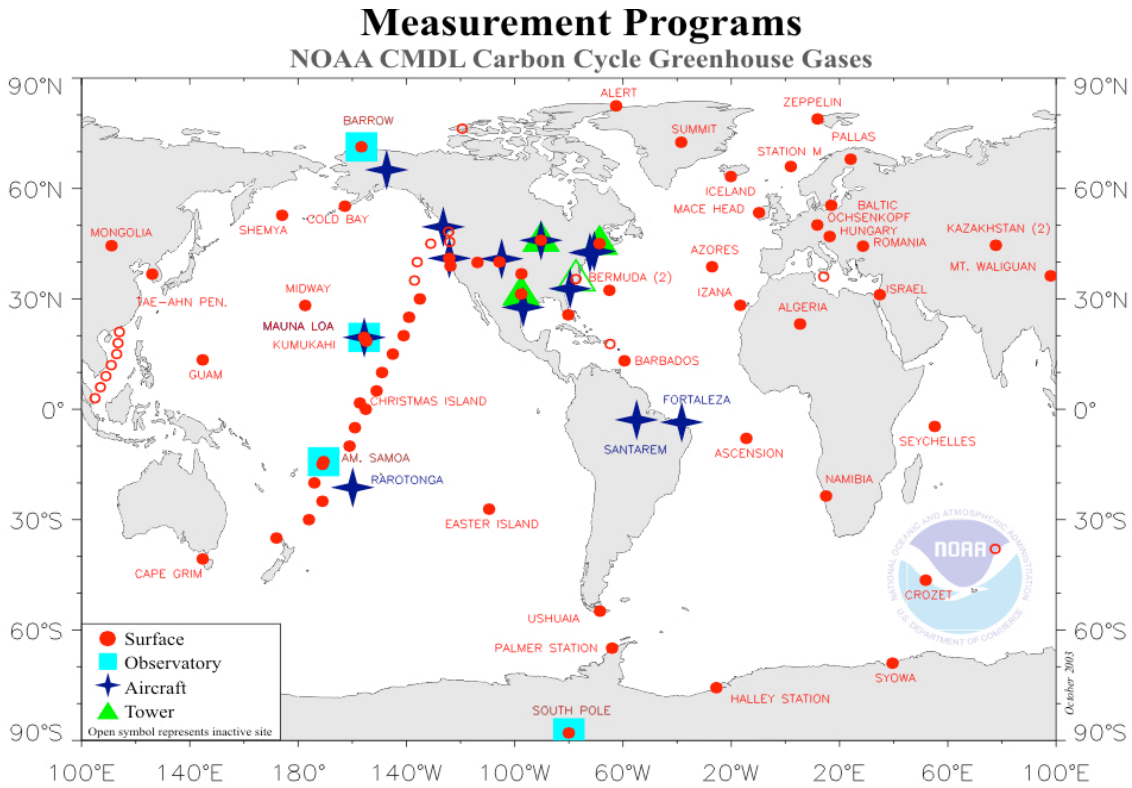

The NOAA CMDL Carbon Cycle Greenhouse Gases group operates 4 measurement programs. In situ measurements are made at the CMDL baseline observatories: Barrow, Alaska; Mauna Loa, Hawaii; Tutuila, American Samoa; and South Pole, Antarctica. The cooperative air sampling network includes samples from fixed sites and commercial ships. Measurements from tall towers and aircraft began in 1992. Presently, atmospheric carbon dioxide, methane, carbon monoxide, hydrogen, nitrous oxide, sulfur hexafluoride, and the stable isotopes of carbon dioxide and methane are measured. Group Chief: Dr. Pieter Tans, Carbon Cycle Greenhouse Gases, Boulder, Colorado, (303) 497-6678 (pieter.tans@noaa.gov, http://www.cmdl.noaa.gov/ccgg).

Figure 2. NOAA/CMDL measurement program for carbon cycle greenhouse gases.

The process uncertainties could be reduced with more of these campaigns and additional measurements over the continents, but in reality these operations are difficult to set in motion, cannot accommodate all political and geographic barriers, and are unlikely to achieve the kind of global coverage and constraint that can offer great progress in understanding for the next decade.

In 1992, NOAA CMDL began taking measurements from tall television transmission towers and found this to be a reasonable way to sample over the continents without the problems of boundary layer variability *[Bakwin et al., 1995]*. The effort to establish more continental observing stations is now growing due to evidence that the concentration footprint of these tall tower measurements is sufficient for global model resolution *[Gloor et al., 2001]*.

Following this need for greater reduction in uncertainty on carbon flux estimates, together with the evidence that tall tower measurements are a reasonable way to capture regional fluxes on the continents, I investigated whether creating networks of "virtual" tall towers, by proxy with shorter flux towers, could accomplish this task to further constrain the surface observational network as determined by use in inversions of global transport models.

CHAPTER 2. BACKGROUND

2.1 Tracer Transport Inversions

Inverse modeling is a useful tool for estimating the strength of surface carbon sources and sinks. In this technique, surface carbon fluxes are estimated from empirical observations that incorporate spatial and temporal patterns in the atmosphere. This involves using inverse calculations of atmospheric transport. A synthesis inversion can accomplish this task by using the information from atmospheric observations together with *a priori* flux estimates that are constructed from ground-based observations. *A priori* fluxes contain "prior" information about the ocean-atmosphere carbon exchange, land-atmosphere exchange, and fossil fuel emissions. Unit emissions are prescribed in specific spatial and temporal patterns and scaled by the inversion in space and time resulting in "basis functions" [*Enting, 2002*]. They are scaled to match the measured CO_2 using a backwards or "inverse" calculation. Sub-regional patterns of fluxes associated with each basis function are prescribed as hard constraints, so the inversion is not allowed to adjust the emission spatial distribution in this way. The resulting time-varying mixing ratios that arise in the transport model from the basis functions represent the flux field and are referred to as "response functions". Linear combinations of the response functions are used to reconstruct timeseries of CO_2 concentrations.

The inverse method is based upon the idea that the change in tracer concentration is due to advection of air parcels in time and sources and sinks that influence those air parcels as they are transported over various surface conditions. This can be illustrated simply in time-varying mathematical form by the following equation:

$$\frac{\partial}{\partial t}(\rho C) = -\nabla \cdot (\rho C \vec{V}) + S_C \tag{1}$$

where

C = concentration (observed by measurements)

$\vec{V}$ = transport (modeled by general circulation models (GCMs))

S_C = carbon sources and sinks (solved for using inverse calculations)

A particular observed concentration is defined as being the product of the transport and source of all relevant emissions. This relationship is defined in the following equation:

$$\vec{d} = \hat{G}\vec{m} \tag{2}$$

where

$\vec{d}$ = observed concentration data
$\hat{G}$ = Jacobian matrix of transport operator
$\vec{m}$ = flux

The simulated GCM responses to the fluxes are the same "response functions" referred to earlier and are organized into a Jacobian matrix of information that describes all types of emissions being considered.

In inverse methods, this matrix is commonly referred to as the *G matrix* ($\hat{G}$). Were Equation (2) and its matrices expanded in scalar form, it would appear:

$$\begin{bmatrix} d_1 \\ d_2 \\ d_3 \\ . \\ . \\ d_N \end{bmatrix} = \begin{bmatrix} G_{11} & G_{12} & G_{13} & . & . & G_{1M} \\ G_{21} & G_{22} & G_{23} & . & . & G_{2M} \\ G_{31} & G_{32} & G_{33} & . & . & G_{3M} \\ . & . & . & . & . & . \\ . & . & . & . & . & . \\ G_{N1} & G_{N2} & G_{N3} & . & . & G_{NM} \end{bmatrix} \begin{bmatrix} m_1 \\ m_2 \\ m_3 \\ . \\ . \\ m_M \end{bmatrix}$$

where

$$d_1 = G_{11}m_1 + G_{12}m_2 + ...G_{1M}m_M$$

$d_1 =$ observed concentration at location 1

$G_{12} =$ partial derivative of concentration at location 1 with respect to type 2 CO_2 emissions

$m_1 =$ emissions of type 1

If the problem were simple and the *G matrix* was square, the solution to Equation (2) would be easy:

$$\vec{m} = \hat{G}^{-1}\vec{d} \tag{3}$$

where

$\hat{G}^{-1}$ = inverse of the *G matrix*

Since this is a very ill-conditioned problem – meaning that there are many more unknown variables than equations that can be used to find solutions, we cannot use a simple matrix inversion. $\hat{G}^{-1}$ doesn't exist. But there is a solution.

To obtain optimal estimates of the regional monthly sources and sinks, m_{est} , we use a least-squares technique of defining a **cost function**, *S*, which penalizes deviation of

the modeled concentrations from the data and deviations of the fluxes from prior estimates [*Tarantola, 1987*].

The cost function is defined in this way:

$$S(\vec{m}_{est}) = [(\hat{G}\vec{m}_{est} - \vec{d}_{obs})^t \hat{C}_d^{-1} (\hat{G}\vec{m}_{est} - \vec{d}_{obs}) + (\vec{m}_{est} - \vec{m}_p)^t \hat{C}_m^{-1} (\vec{m}_{est} - \vec{m}_p)] \quad (4)$$

where

$\hat{G}$ = *G matrix* of response functions
$\vec{m}_{est}$ = final flux estimate
$\vec{m}_p$ = *a priori* flux estimate
$\vec{d}_{obs}$ = observed concentration data
$\hat{C}_d^{-1}$ = data uncertainty
$\hat{C}_m^{-1}$ = *a priori* flux estimate uncertainty

The first term on the right-hand side of Equation (4) refers to mismatch between the model and the data. The second term on the right-hand side refers to the deviation of inferred fluxes from the priors. C_d is a covariance matrix of the observational data vector d_{obs}. (C_d is not shown in Equation (4).) The inverse of C_d, or C_d^{-1}, is a covariance matrix that is constructed with a diagonal of $(1/C_d)^2$ to give weight, or confidence level, to the observational data values. The diagonal elements are the only non-zero elements in this matrix. C_m (not shown in Equation (4)) is the *a priori* flux estimate uncertainty covariance matrix, and the inverse of C_m, or C_m^{-1}, is the *a priori* covariance matrix with a diagonal of $(1/C_m)^2$ to give weight, or confidence level, to the *a priori* flux estimates. Similarly, the non-diagonal elements in this matrix are zero.

The equation to solve is:

$$\frac{\partial S}{\partial \vec{m}_{est}} = 0 \quad ; \quad \text{solve for } \vec{m}_{est} \tag{5}$$

Following *Tarantola* [1987], the solution of flux magnitudes ($\vec{m}_{est}$) that minimizes the cost function is:

$$\vec{m}_{est} = \vec{m}_p + (\hat{G}^t \hat{C}_d^{-1} \hat{G} + \hat{C}_m^{-1})^{-1} \hat{G}^t \hat{C}_d^{-1} (\vec{d}_{obs} - \hat{G}\vec{m}_p) \tag{6}$$

where

$\hat{G}$ = *G matrix* of response functions
$\hat{G}^t$ = transpose of *G matrix*
$\vec{d}_{obs}$ = observed concentration data
$\vec{m}_{est}$ = final flux estimate
$\vec{m}_p$ = *a priori* flux estimate
$\hat{C}_d^{-1}$ = data uncertainty
$\hat{C}_m^{-1}$ = *a priori* flux uncertainty

and the term:

$$C_m^* = (\hat{G}^t \hat{C}_d^{-1} \hat{G} + \hat{C}_m^{-1})^{-1} \tag{7}$$

represents the *a posteriori* estimate of uncertainty in the fluxes. Equation (7) does not depend on observations per se. There are no flux or data estimates in this term, only flux and data estimate uncertainties. This is a linear system and thus singular value decomposition (SVD) technique was used to find the least-squares solution for these large matrices.

The *a posteriori* uncertainty estimate in Equation (7) is an important parameter in this research. The objective is to determine whether networks of virtual tall towers can add enough information to be meaningful for constraining the carbon budget, and consequently what network is optimal for providing this information. The *a posteriori* uncertainty estimates are important because they demonstrate how much information has been added to the inversion. Therefore, this term is a focal point as an important measure for whether these objectives have been met and I investigated how C_m^* changed according to inversions of different configurations of modeled virtual tall tower networks. This approach does not offer more information or improve estimates of carbon flux, only estimates of uncertainty that are associated with that flux.

2.2 Previous Inversion Studies

Previous inversion studies have produced some intriguing results about carbon sources and sinks. *Rayner et al.* [1999] used Bayesian synthesis inversion to investigate the spatial-temporal patterns of CO_2 fluxes to the atmosphere during the years 1980-1995 using measurements of atmospheric concentration and isotopic composition. *Bousquet et al.* [2000] used an inverse model with 20 years of atmospheric CO_2 measurements to analyze interannual variations in regional carbon balance of oceans and continents. They determined that tropical ecosystems have contributed the most to yearly changes in the carbon budget for the last 20 years. Both Rayner [1999] and Bousquet [2000] neglected interannual variability of atmospheric transport. More recently, *Gurney et al*. [2002] applied an inverse model to 16 atmospheric tracer transport models to determine regional

CO_2 sources and sinks. They found a northern hemisphere land sink and a southern extratropical ocean uptake to be weaker than previously estimated. They also concluded that for less problematic errors in inversions, further constraints are needed in the form of better transport models and a more extensive tropical CO_2 surface observational network. More recently, *Roedenbeck et al.* [2003] investigated the effects of using interannually-varying transport in global time-dependent inversions for CO_2 sources and sinks.

My research project made use of a recent collaboration between atmospheric tracer transport modelers, that began in 1993 to determine the effects of different transport modeling schemes on inverse surface carbon flux estimations. The Atmospheric Tracer Transport Intercomparison Project – referred to as "Transcom", was a project of the International Geosphere-Biosphere Progamme's (IGBP) Global Analysis Interpretation and Modeling (GAIM) Project. The experimental protocol prescribed background fluxes for fossil fuel emissions, net ecosystem production (NEP) according to ecosystem model parameters of net primary production (NPP), and atmosphere-ocean exchange [*Gurney et al., 2000*]. Transcom divided the world into 11 land regions and 11 ocean regions based loosely on vegetation characteristics derived from Normalized Differential Vegetation Index (NDVI) data that are retrieved from an advanced very high resolution radiometer (AVHRR) instrument aboard a low Earth orbiting satellite. The partitioning of these 22 regions can be seen in **Figure 3**. Regional fluxes from these partitions are considered in addition to the prescribed fluxes in order to correct the surface flux distribution in the inversion to optimize the gap between the model and observed data.

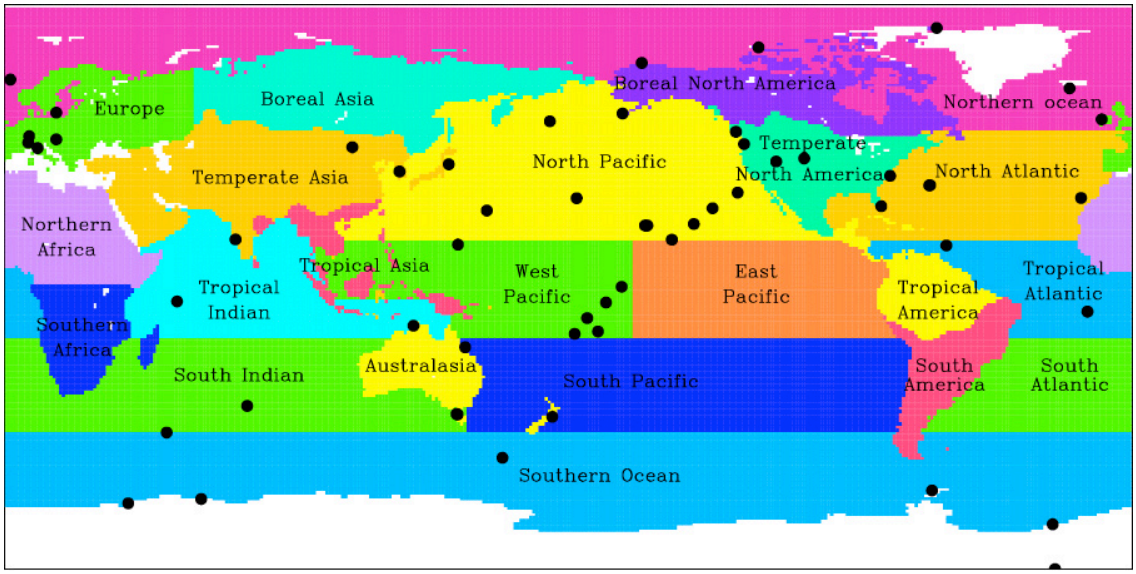

Figure 3. The partitioning of 22 Land and Ocean regions of the Transcom Project.

(Black dots represent sites in the flask measurement network.)

Twelve different global tracer transport models were used by the Transcom modelers to produce CO_2 concentration response functions to 264 prescribed unit emission pulses – one pulse for each month for each region. In the third phase of the Transcom experiment (hereafter referred to as Transcom3), surface-atmosphere CO_2 fluxes were estimated from atmospheric CO_2 inversion models. They showed a discrepancy between the predicted Southern Ocean fluxes in this inversion and those reported in the global database of CO_2 partial pressure (pCO_2). This study estimated carbon uptake in the southern extratropics to be about half of that based on the pCO_2 database, and showed that new measurements would be most useful if taken from the South American and southern Atlantic Ocean regions, while also sampling the tropical

continents [*Gurney et al., 2003*]. **Table 2** shows the models associated with Transcom3 and their various parameters.

Table 2. The twelve global tracer transport models used in the Transcom3 inversions.

Model	Modeller	Type	Horizontal Resolution	Vertical Resolution	Advection	Wind	Freq	Sub-grid scale				
								Hdiff	Vdiff	Conv	Turb	PBL
ANU	Taylor	Off	2.5°	7 pressure	lagrangian	ECMWF(80)	Stats	Y	Y	-	-	-
CSIRO9	Watterson	On	3°×5.6°	9 sigma	semi-lag	-	-	-	-	Y	Y	-
CSU	Denning	On	4°×5°	17 sigma	2nd order	-	-	-	-	Y	Y	Y
GFDL	Rayner	Off	265 km	11 sigma	2,4 order	GFDL GCM	6 hr	Y	Y	-	-	-
GISS	Trudinger	Off	8°×10°	9 sigma	slopes	GISS GCM	4 hr	Y	-	Y	-	-
MUGCM	Law	On	R21	9 sigma	spectral	-	-	Y	Y	Y	-	-
MUTM	Law	Off	R21	9 sigma	spectral	MU GCM	24 hr	Y	Y	Y	-	-
NCAR	Erickson	On	2.8°	18 sigma	semi-lag	-	-	-	Y	Y	-	Y
NIRE	Taguchi	Off	2.5°	15 sigma	semi-lag	ECMWF(92)	6 hr	-	-	-	-	Y
TM1	Piper	Off	8°×10°	9 sigma	slopes	ECMWF(79)	12 hr	Y	-	Y	-	-
TM2	Heimann	Off	4°×5°	9 sigma	slopes	ECMWF(86)	12 hr	-	Y	Y	-	-
TM2Z	Ramonet	Off	2.5°	9 sigma	slopes	ECMWF(90)	12 hr	-	Y	Y	-	-

2.3 Previous Optimization Studies

Simulated annealing (SA) is a common approach to network optimization and was used by *Rayner et al.* [1996] and *Gloor et al.* [2000] to determine which sampling sites would further optimize the CO_2 observational network for the purpose of reducing uncertainty on estimates of carbon flux. The SA technique is modeled after the simulation of a crystal lattice that reaches minimum energy states while changing phase. Using this method, *Rayner et al.* [1996] concluded that the next single best step to make was to take measurements in tropical South America.

Noting that SA is computationally expensive and probabilistic, *Patra et al.* [2002] used an algorithm known as Incremental Optimization (IO) to investigate which various network configurations most reduced uncertainty of flux estimates through the process of adding new station sites one by one. New individual site selection was based on the level of positive flux estimate uncertainty reduction achieved by that specific addition. This algorithm is less computationally expensive, more deterministic – resulting in a unique solution, more simple to implement, and performs equally well or better than SA. Using this method they were able to reduce total CO_2 flux uncertainty estimates by 59%, 47%, 35%, and 29% with additions of 3, 5, 12, and 20 stations, respectively, as relative to a reference network. Their results indicated that the most poorly constrained regions for inverse models were tropical America, South America, tropical Africa and South Africa. Their results also emphasized that more CO_2 measurements are especially needed over the continental areas of Africa, South America, and Asia.

These studies neglected to consider which global grid cells were realistically feasible to sample. Therefore, their results are useful to consider as an academic exercise but become moot when trying to implement the deduced strategies in reality.

2.4 Virtual Tall Tower Theory

Based on these previous inversion studies, there is clearly a need for more terrestrial measurement stations around the world. The continental regions suffer most

from lack of observations, due to difficulties in measuring where landscape heterogeneity, strong vertical gradients, and dynamic diurnal cycles persist. Tall towers try to avoid these difficulties by measuring in the mixed-layer, but they are very expensive to implement and maintain [*Bakwin et al., 1995*], [*Davis et al., 2001*]. The measurements of shorter surface-layer flux towers would be reasonable to use if they could be extrapolated to represent mixed-layer CO_2 concentrations. Flux towers that currently operate take measurements in the canopy surface layer while the grid cells of global circulation models represent measurements from the higher mixed-layer. In order to harmonize real observations and theoretical models there must be a reconciliation between these disparate representations. "Virtual" tall towers can be constructed using measurements of calibrated [CO_2] and fluxes from short towers [*Davis et al., 2003*], in a methodology that is currently being tested at a real tall tower in Wisconsin.

Previous studies in optimization of carbon observing networks considered any global grid cell as eligible for selection as a measurement site [*Patra et al., 2002*], [*Gloor et al., 2000*], [*Rayner et al., 1996*]. In reality, measurement of mean CO_2 over highly variable terrestrial regions is very impractical and expensive. A global network of eddy-covariance flux towers already exists in which continuous measurements of CO_2 are taken, as well as measurements of sensible heat (H) and latent heat (LE), such that net ecosystem exchange (NEE) can be estimated. If the CO_2 measurements were calibrated, these surface-layer values could be extrapolated to the mixed-layer using similarity theory providing a means to sample the continental mixed-layer for use in global inversions to further constrain the carbon budget. With this method for estimating the

mid-day continental boundary layer CO_2 from calibrated CO_2 and eddy-covariance measurements at flux towers, a network of virtual tall towers (hereafter referred to as *VTT*) could be readily implemented using existing infrastructure and minimal additional instrumentation. In this way, the ill-conditioning of having a network that is too sparse to deduce global fluxes can be overcome. My research objective is to show that significant uncertainty reductions can be achieved for regional and global estimates of carbon flux using the virtual tall tower method.

The atmospheric planetary boundary layer (PBL) is dominated by turbulent flow and separated by a density inversion from the free atmosphere that is characterized by laminar flow. Air parcels in the boundary layer move over land at approximately 500 km/day during fair weather conditions [*Gloor et al., 2001*]. As meteorological processes circulate these parcels over different ecosystems, the gaseous composition of the parcels is modified by photosynthesis, evapotranspiration, ecosystem respiration, and exchanges of sensible and latent heat. This influence is diluted by synoptic-scale subsidence and frontal passages that induce mixing of boundary layer and free tropospheric air. Thus the resulting air masses that reside over the land surface are a result of the initial composition of air that was entrained from the free troposphere, the ecosystem processes and surface characteristics over which the parcels have passed, and the mesoscale meteorological processes that induced mixing during boundary layer development [*Baldocchi, 2003*].

Boundary layer air over the continents is richer in CO_2 in winter, and poorer in summer, than marine boundary layer air because of the effects of soils, vegetation, and

fossil fuel combustion. During summer, photosynthesis induces a drawdown of CO_2 and during winter when plants are dormant the ecosystems serve as a source of carbon to the boundary layer. The following schematic is a simple height cross-section showing the variable concentration of CO_2 during a well-mixed convective afternoon in the growing season.

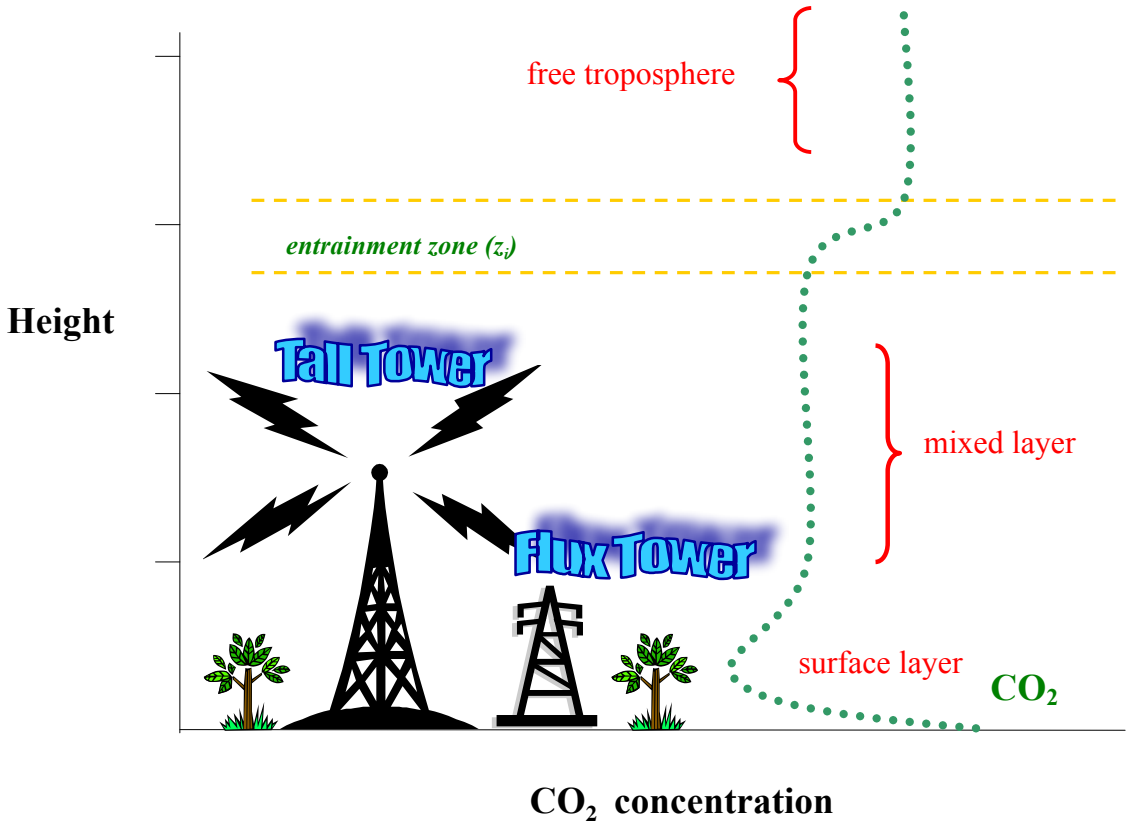

Figure 4. A simple schematic of surface [CO_2] varying with boundary-layer height.

The figure is not drawn to scale, but indicates general trends of the continental boundary layer that is characterized by diurnal cycles and steep vertical gradients which large scale models cannot resolve. Near the surface, the concentration of CO_2 is the highest because the eddies are so small that soil respiration cannot be mixed into the

higher canopy air. As carbon travels higher in the canopy and farther from the surface it experiences more mixing by turbulent eddies.

This methodology has been tested and refined at the WLEF tall tower in northwest Wisconsin, where continuous CO_2 concentration data have been collected since 1995 from heights of 30 m and 396 m above the surface [*Davis et al, 2001*]. The tower is a 447 m television transmission tower located in an unpopulated area of temperate forest. This site participates in an association with similar flux tower sites in North America called "Ameriflux" [http://public.ornl.gov/ameriflux]. Currently all Ameriflux sites take measurements of CO_2 mixing ratios in order to calculate eddy-covariance fluxes of water vapor, sensible heat, and CO_2. However, there is minimal effort to maintain long-term precision and absolute accuracy for [CO_2]. Currently [CO_2] is measured at a frequency of 5-10 Hz at every flux tower, but there is no calibration to primary gas standards and thus the precision can vary by 1-10 ppm, and in a small number of cases – up to 100 ppm [*Julie Styles, personal communication*]. This level of uncertainty is unacceptable because it would produce large errors in retrieved fluxes when propagated through an inversion.

Figure 5 shows a depiction of one month of data from September 1997 at the WLEF tower. In the top panel, the data show that the [CO_2] measurements at 30 m are able to track the synoptic variability observed at 396 m, which varies by ~ 35 ppm during the month. The temperature record clarifies the presence of fronts that correspond to the synoptic pattern.

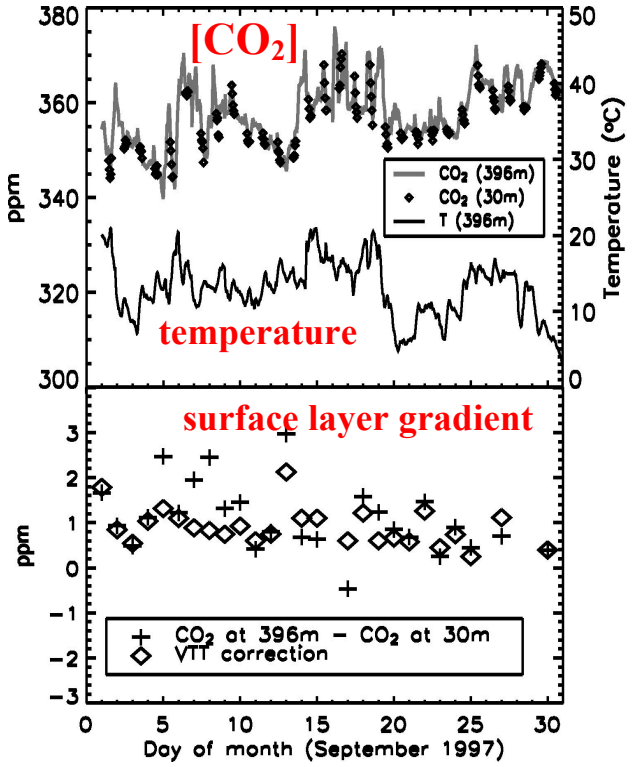

Figure 5. WLEF tower measurements and correction estimates.

Figure courtesy of Dan Ricciuto and Ken Davis

In the bottom panel, turbulent mixing and vertical gradients have been estimated using sensible heat flux and momentum stress measurements, and the predicted [CO_2] is compared to the observed [CO_2] at 396 m. When the VTT correction does not accurately predict the 396 m measurements, there is a tendency for under-predicting. This analysis shows a bias of 0.2 ppm and a variance of 0.2 ppm, which is low enough in the context of the flux that is trying to be captured, and for what is needed in the scope of inversion modeling, to be reasonable for use in global models. By using the monthly means of these data, it is also likely that there is less representation error than the weekly flask

measurements. Another advantage is that the root mean square (rms) error of the monthly mean observations is comparable to analytical error under good conditions. Analytical (or instrument) error is the lowest error that can be achieved in observational data.

The defining equation using mixed-layer similarity theory for this method describes the change in concentration with height as being the result of the entrainment flux subtracted from the surface flux [*Moeng, 1984*], and is described as follows:

Mixed-Layer Similarity Theory

$$\frac{\partial C}{\partial z} = -g_b\left(\frac{z}{z_i}\right)\frac{F_0^C}{w_* z_i} - g_t\left(\frac{z}{z_i}\right)\frac{F_{z_i}^C}{w_* z_i} \qquad (8)$$

where

C = scalar mixing ratio [CO_2]

$\mathbf{F_0^C}$, $\mathbf{F_{zi}^C}$ = surface and entrainment fluxes

z = altitude above ground or displacement height

$\mathbf{z_i}$ = depth of convective boundary layer

w* = convective velocity scale (a function of surface buoyancy flux and z_i)

$\mathbf{g_b}$, $\mathbf{g_t}$ = dimensionless gradient functions, which depend on normalized altitude within the convective layer.

Similarity theory is based on organizing variables into dimensionless groups that have empirical relationships to each other as defined in an equation. This theory does not

tell the form of the equation or the relationship between the dimensionless groups, so physical insight is used to inform the technique. These relationships are usually applied to situations where steady-state is implied, and thus time is not included as a variable. Rather the variables are used to yield equilibrium profiles of mean variables and turbulence statistics as a function of height or position [*Stull, 1994*]. In this case, boundary layer height is variable with time and fluxes are measured by eddy covariance. The mixed-layer [CO_2] is then calculated using gradient functions derived from eddy simulations.

The virtual tall tower theory asserts that 400 m observations can be simulated with 30 m-measurements using mixed-layer similarity theory to estimate the surface gradient [*Davis, 2003*]. This is done using surface-layer flux and mixing ratio data that infers the CO_2 mixing ratio in the mixed layer. This gradient can be estimated during mid-day convective conditions accurately enough to simulate 400 m observations for use in global inverse models. The VTT method is believed to work best in the mid-afternoon because the gradient is less steep and easier to estimate than it would be at night while experiencing the surface stable layer and nocturnal tropospheric jet [*Davis et al., 2003*].

Ameriflux is part of a greater worldwide network of monitoring stations referred to as FLUXNET (**Figure 6)**. This represents a global network of process observatories all currently using eddy covariance to estimate sensible heat (H), latent heat (LE), and net ecosystem exchange (NEE) [*Ameriflux, 2003*].

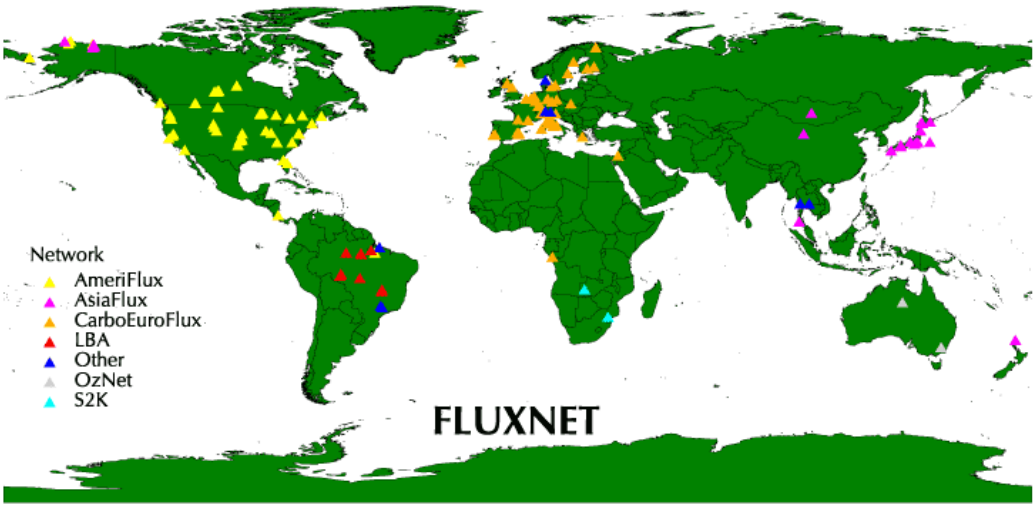

Figure 6. The FLUXNET network of global flux measurement sites.

Each of these sites is also collecting uncalibrated continuous CO_2 concentration data, as are Ameriflux sites. If these data could be used in inverse models, the number of [CO_2] measurement sites would more than double and in fact be quite dense over some continental areas. With implementation of an additional trace gas sensor, calibration gases, and some technical expertise, accurate [CO_2] measurements can be taken using existing infrastructure and be readily available for use in VTT methodology [*Ken Davis, personal communication*].

The purpose of this study is to investigate to what degree incorporating precise virtual tall tower [CO_2] data into global inverse models would reduce global and regional estimates of carbon fluxes, and to determine if this would further constrain the continental regions that currently persist as a problem to global optimization.

CHAPTER 3. METHODS

3.1 Introduction

I used twelve tracer transport models from Transcom3 to do inversions of regional and global virtual tall tower networks, as created from selections of mid-afternoon measurments in high-frequency timeseries data saved from the forward runs of these same models. At first, I created these networks by hand based on heuristic judgments about strategies that might work for capturing the continental carbon flux for North America. I tested many of these networks in the inversions and compared them to each other to gain an understanding of which strategies were most efficient in reducing uncertainty. Then I used a deterministic genetic algorithm to find a specific network solution for both the North America and global inversions.

The cyclostationary inversion code used is a general Bayesian time-dependent inverse solver that operates on input data of trace gas records in terms of a series of pulsed sources with predetermined spatial structure. The inversion is described as being "cyclostationary" because of the periodically varying or quasi-stationary nature of the seasonal cycle of CO_2 about an annual mean. The input data are the Green's function responses for each source, where the Green's functions have been pre-calculated by inserting pulses of that source into an atmospheric transport model. Also included in the

input data is a series of prior estimates for the time histories of each source and covariances for these estimates.

The actual CO_2 fluxes are transported by the circulating atmosphere and then influence concentrations in time and space. By the time these concentrations are detected with empirical networks there has already been an attenuation of information. Timeseries are made from observations of the concentrations, which are then used in an inverted transport model to estimate the original sources and sinks. During this inverse process to estimate the sources, the errors are amplified. Thus, large errors that exist before the inversion will become a problem and the process will not provide a meaningful solution.

The flux observations were prescribed as a weak constraint with estimated uncertainties. How far the fluxes can deviate from this information is controlled, and solutions that produce unreasonable values were penalized. Each of these constraints was weighted with uncertainties that determine the magnitude of their contribution to minimizing the cost function (*see chapter 1*).

In the inversion setup for my experiments there are 269 basis functions (*see chapter 1*), which are constructed as:

264 **initial basis functions** (= regions [22] *x* months [12])
+ 4 **background fluxes** (pre-subtracted fields)
+ 1 **background offset** (global mass-balance constraint)

= 269 **total basis functions**

The background fluxes are referred to as pre-subtracted fields, or "pre-subtracts", because the modeled concentration responses corresponding to these prior background fluxes are subtracted from the monthly concentrations before the inversion is performed. The inversion acts only on the residual concentrations. They consist of four *a priori* fields of seasonal terrestrial biosphere exchange, ocean-atmosphere gas exchange, and two fossil fuel emission fields. The seasonal terrestrial biosphere exchange, or net ecosystem production (NEP), is derived from the Carnegie Ames Stanford Approach (CASA) ecosystem model [*Randerson et al., 1997*] and is annually balanced for a zero net flux in every grid cell. The monthly mean global air-sea exchange is prescribed with seasonal variation and an annual oceanic uptake of 2.19 Gt C yr^{-1} from measurements of partial pressure differences (ΔpCO_2) by *Takahashi et al.* [1999]. The fossil fuel emission fields are annual mean sources (no seasonality) that are derived from 1990 [*Andres et al., 1996*] and 1995 [*Brenkert et al., 1998*] data records and total 5.812 Gt C yr^{-1}, and 6.173 Gt C yr^{-1}, respectively. Flux estimate uncertainties were calculated for every month of the year for every region, totaling 264 uncertainty values associated with the 264 initial basis functions. The basis functions were scaled to match the measured CO_2 using a backwards or "inverse" calculation.

Using this technique, monthly mean estimates of regional fluxes and uncertainties were generated using Equation (7) across the 1992-1996 time period for the same set of stations used in the Transcom1 annual mean inversion plus additional tower sites that are assigned fictional observations and uncertainties.

Mid-day sampling of the high-frequency timeseries global fields generated by forward runs of the transport models was done by sampling from the hour closest to 2 pm local time. These samples were then turned into monthly mean response functions before the inversion. From all three years of high-frequency model output, the concentration response that corresponded to mid-day at each station was selected for the purpose of sampling in the mid-afternoon only, when VTT theory works best. Then each daily sample was averaged to obtain a monthly mean, mid-day, mid-PBL value.

The 245 station list is composed of the 228 Transcom3 Level 2 control stations and the additional 17 Pacific Ocean stations, and follows in **Table 3** (*Gurney et al., 2000*). This list includes the 75 flask stations.

Table 3. The 245 station list used in the Transcom3 Level 2 experiment.

Station	latitude	longitude	elev (m)	type1[1]	type2[2]	Direction	NS
GLOBALVIEW[3]							
Bass Strait/Cape Grim	-40.38	144.39	500	a	O	SW	NS
Bass Strait/Cape Grim	-40.38	144.39	1500	a	O	SW	NS
Bass Strait/Cape Grim	-40.38	144.39	2500	a	O	SW	NS
Bass Strait/Cape Grim	-40.38	144.39	3500	a	O	SW	NS
Bass Strait/Cape Grim	-40.38	144.39	4500	a	O	SW	NS
Bass Strait/Cape Grim	-40.38	144.39	5500	a	O	SW	NS
Bass Strait/Cape Grim	-40.38	144.39	6500	a	O	SW	NS
Alert, Greenland	82.45	-62.52	210	u	O	SW	
Amsterdam Island	-37.95	77.53	150	f	O		
Ascension Island	-7.92	-14.42	54	f	O		
Assekrem, Algeria	23.18	5.42	2728	f	L		NS
St. Croix, Virgin Is.	17.75	-64.75	3	f	O		
Azores	38.75	-27.08	30	f	O		
Baltic Sea, Poland	55.50	16.67	7	f	O		
Baring Head St., NZ	-41.41	174.87	80	u	O	S,SW	
Bermuda West	32.27	-64.88	30	f	O		
Barrow, Alaska	71.32	-156.60	11	u	O	E,NE	
Black Sea, Romania	44.17	28.68	3	u	O	NE	
Carr, CO	40.90	-104.80	3000	a	L		NS
Carr, CO	40.90	-104.80	4000	a	L		NS
Carr, CO	40.90	-104.80	5000	a	L		NS
Carr, CO	40.90	-104.80	6000	a	L		NS
Cold Bay, Alaska	55.20	-162.72	25	f	O		

[1] "a" - aircraft, "u" - continuous analyzer, "f" - flask, "t" - tower.

[2] "O" = ocean, "L" - land.

[3] The Pacific Ocean ship measurements were eliminated from the high-frequency reporting because it is unlikely they would differ much from the monthly means which are reported for every gridcell.

Cape Ferguson, Aust.	-19.28	147.06	2	u	O	E	
Cape Grim, Tasmania	-40.68	144.68	94	u	O	SW	
Christmas Island	1.70	-157.17	3	f	O		
Mt. Cimone St., Italy	44.18	10.70	2165	f	L		NS
Cape Meares, OR	45.48	-123.97	30	u	O	W,NW	
Cape Rama, India	15.08	73.83	60	u	O	S,SE	
Crozet, Indian Ocean	-46.45	51.85	120	f	O		
Cape St. James, Canada	51.93	-131.02	89	u	O	W	
Darwin, Australia	-12.42	130.57	3	u	O	W,NW	
Easter Island	-29.15	-109.43	50	f	O		
Estevan Pt, BC, Canada	49.38	-126.55	39	u	O	W	
Guam	13.43	144.78	2	f	O		
Dwejra Pt., Malta	36.05	14.18	30	f	O		
Halley Bay, Antarctica	-75.67	-25.50	10	f			
Hungary	46.95	16.65	300	t	L		
Storhofdi, Iceland	63.25	-20.15	100	f	O		
North Carolina	35.35	-77.38	60	t	L		
North Carolina	35.35	-77.38	500	t	L		NS
Canary Islands	28.30	-16.48	2360	f	O		NS
Jubany St., Antarctica	-62.23	-58.82	15	f			
Key Biscayne, FL	25.67	-80.20	3	u	O	S	
Kosan, Rep. of Korea	33.28	126.15	72	u	O		
Kumukahi, Hawaii	19.52	-154.82	3	f	O		
Wisconsin tower	45.93	-90.27	500	t	L		NS
Wisconsin tower	45.93	-90.27	850	t	L		NS
Lampedusa, Italy	35.52	12.62	85	f	O		
Mawson St., Antarctica	-67.62	62.87	32	f			
Mould Bay, Canada	76.25	-119.35	58	f	O		
Sand Island, Midway	28.22	-177.37	4	f	O		
Mauna Loa, Hawaii	19.53	-155.58	3397	f	O		NS
Minamitorishima, Japan	24.30	153.97	8	f	O		
Macquarie Island	-54.48	158.97	12	f	O		
Olympic Peninsula, WA	48.25	-124.42	488	u	O	W	
Plateau Rosa St., Italy	45.93	7.70	3480	f	L		NS
Palmer St., Antarctica	-64.92	-64.00	10	f			
Qinghai Province, PRC	36.27	100.92	3810	f	L		NS
Ragged Pt., Barbados	13.17	-59.43	3	f	O		
Ryori St., Japan	39.03	141.83	230	u	O	E	
Schauinsland, Germany	48.00	8.00	1205	f	L		NS
South China Sea	3.00	105.00	15	f	O		
South China Sea	6.00	107.00	15	f	O		
South China Sea	9.00	109.00	15	f	O		
South China Sea	12.00	111.00	15	f	O		
South China Sea	15.00	113.00	15	f	O		
South China Sea	18.00	115.00	15	f	O		
South China Sea	21.00	117.00	15	f	O		
Sable Island, NS, Can.	43.93	-60.02	5	u	O	E	
Mahe Island, Seychelles	-4.67	55.17	3	f	O		
Shemya Island, Alaska	52.72	174.10	40	f	O		
Shetland Is., Scotland	60.17	-1.17	30	f	O		
Samoa	-14.25	-170.57	42	f	O		
South Pole	-89.98	-24.80	2830	f			
Atlantic Ocean, Norway	66.00	2.00	7	f	O		
Pacific Ocean, Canada	50.00	-145.00	7	f	O		
Syowa, St., Antarctica	-69.00	39.58	11	f			
Tae-ahn Pen., Korea	36.73	126.13	20	u	O		
Wendover, Utah	39.90	-113.72	1320	f	L		
Ulaan Uul, Mongolia	44.45	111.10	914	f	L		
Westerland, North Sea	55.00	8.00	8	u	O	W	
Sede Boker, Israel	31.13	34.88	400	u	O	NW	
Zeppelin St., Norway	78.90	11.88	474	f	O		
FLUX TOWERS							
amer.ca01flan.01	49.60	-112.60	951	t	L		
amer.ca01roul.01	45.41	-75.52	-999	t	L		
amer.ca02vanc.01	49.85	-125.32	300	t	L		
amer.ca03born.01	55.90	-98.50	259	t	L		
amer.ca08cmpb.01	44.32	-79.93	120	t	L		
amer.ca11sbor.05	53.90	-104.70	579	t	L		
amer.cs00lase.01	10.43	-83.98	200	t	L		
amer.usakhapp.01	69.13	-148.83	366	t	L		
amer.usakupad.01	70.27	-148.88	3	t	L		

amer.uscajasp.01	37.40	-122.22	100	t	L		
amer.uscaskyo.01	33.37	-116.62	1420	t	L		
amer.usflcypr.01	29.73	-82.08	50	t	L		
amer.usilbond.01	40.00	-88.29	213	t	L		
amer.uskskonz.01	39.12	-94.35	324	t	L		
amer.usmaharv.01	42.54	-72.18	300	t	L		
amer.usmdsmit.01	38.88	-76.55	11	t	L		
amer.usmehowl.01	45.25	-68.75	60	t	L		
amer.usmiumbs.01	45.58	-84.70	234	t	L		
amer.usncduke.01	35.87	-79.98	163	t	L		
amer.usokliww.01	34.96	-97.98	-999	t	L		
amer.usorjunp.01	44.27	-121.38	945	t	L		
amer.ustnwalk.01	35.95	-84.28	365	t	L		
amer.uswawind.01	45.82	-121.97	355	t	L		
amer.uswipark.01	45.92	-90.27	470	t	L		
aust.as00warr.01	-19.93	134.60	336	t	L		
euro.be00bras.01	51.30	4.52	10	t	L		
euro.be00viel.01	50.30	6.00	450	t	L		
euro.da00lill.01	55.49	11.65	40	t	L		
euro.fi00hyyt.01	61.85	24.28	181	t	L		
euro.fr00brdx.01	44.08	0.08	60	t	L		
euro.fr00sarr.01	48.67	7.08	300	t	L		
euro.gm00bayr.01	50.15	11.87	780	t	L		
euro.gm00thar.01	50.97	13.63	380	t	L		
euro.it00cast.01	41.75	12.37	3	t	L		
euro.it00coll.01	41.87	13.63	1550	t	L		
euro.nl03wist.01	52.17	5.74	25	t	L		
euro.sw00flak.01	64.12	19.45	225	t	L		
euro.sw00noru.01	60.08	17.47	45	t	L		
euro.uk00aber.01	56.62	-3.80	340	t	L		
flux.br00sugr.01	-21.10	-48.07	520	t	L		
flux.gm00soll.01	57.77	9.58	505	t	L		
flux.it00reno.01	46.59	11.43	1750	t	L		
flux.ja00toma.01	42.59	141.59	75	t	L		
flux.th27sakr.01	14.49	101.92	530	t	L		
flux.th50mark.01	14.59	98.86	170	t	L		
jpan.ja00jawa.01	35.90	139.50	30	t	L		
jpan.ja00tsuk.01	36.02	140.12	20	t	L		
jpan.ja09taka.01	36.13	137.42	1420	t	L		
lbaf.br00biol.01	-2.59	-60.12	90	t	L		
mede.fr00berb.01	43.73	3.58	250	t	L		
mede.gr00gree.01	38.00	22.62	840	t	L		
mede.it14sard.01	40.60	8.15	74	t	L		
mede.po00jarv.01	38.63	-8.60	230	t	L		
mede.sp00unkn.01	38.77	0.25	-999	t	L		
ALEGAGE							
Adrigole, Ireland	52.00	-10.00	50	u	O	SW	
Fraserdale,Ontario, Can.	49.88	-81.57	210	f	L		
Kitt Peak, AZ	31.90	-111.60	2090	f	L		NS
Lauder, NZ	-45.00	169.70	370	u	O	S	
Neumayer, Antarctica	-71.60	-8.30	16	f			
Scripps Pier, CA	32.83	-117.27	14	u	O	W	
Table Mtn., CA	34.40	-117.70	2258	f	L		NS
Trinidad Head, CA	41.05	-124.15	109	u	O	W	
AIRCRAFT							
Tokyo-Syd aircraft	30.00	145.00	10500	a	O		NS
Tokyo-Syd aircraft	25.00	145.00	10500	a	O		NS
Tokyo-Syd aircraft	20.00	145.00	10500	a	O		NS
Tokyo-Syd aircraft	15.00	145.00	10500	a	O		NS
Tokyo-Syd aircraft	10.00	145.00	10500	a	O		NS
Tokyo-Syd aircraft	5.00	145.00	10500	a	O		NS
Tokyo-Syd aircraft	0.00	145.00	10500	a	O		NS
Tokyo-Syd aircraft	-5.00	145.00	10500	a	O		NS
Tokyo-Syd aircraft	-10.00	145.00	10500	a	O		NS
Tokyo-Syd aircraft	-15.00	145.00	10500	a	O		NS
Tokyo-Syd aircraft	-20.00	145.00	10500	a	L		NS
Tokyo-Syd aircraft	-25.00	145.00	10500	a	L		NS
Tokyo-Syd aircraft	-30.00	145.00	10500	a	L		NS
Fyodorovskoye	56.00	33.00	500	a	L		NS
Fyodorovskoye	56.00	33.00	1500	a	L		NS
Fyodorovskoye	56.00	33.00	2500	a	L		NS

Fyodorovskoye	56.00	33.00	3500	a	L	NS
Fyodorovskoye	56.00	33.00	5000	a	L	NS
Syktyvkar	62.00	51.00	500	a	L	NS
Syktyvkar	62.00	51.00	1500	a	L	NS
Syktyvkar	62.00	51.00	2500	a	L	NS
Syktyvkar	62.00	51.00	3500	a	L	NS
Syktyvkar	62.00	51.00	5000	a	L	NS
Zotino	60.00	89.00	500	a	L	NS
Zotino	60.00	89.00	1500	a	L	NS
Zotino	60.00	89.00	2500	a	L	NS
Zotino	60.00	89.00	3500	a	L	NS
Zotino	60.00	89.00	5000	a	L	NS
Surgut	61.00	73.00	500	a	L	NS
Surgut	61.00	73.00	1500	a	L	NS
Surgut	61.00	73.00	2500	a	L	NS
Surgut	61.00	73.00	3500	a	L	NS
Surgut	61.00	73.00	5000	a	L	NS
Norilsk	69.00	88.00	500	a	L	NS
Norilsk	69.00	88.00	1500	a	L	NS
Norilsk	69.00	88.00	2500	a	L	NS
Norilsk	69.00	88.00	3500	a	L	NS
Norilsk	69.00	88.00	5000	a	L	NS
Kirensk	58.00	108.00	500	a	L	NS
Kirensk	58.00	108.00	1500	a	L	NS
Kirensk	58.00	108.00	2500	a	L	NS
Kirensk	58.00	108.00	3500	a	L	NS
Kirensk	58.00	108.00	5000	a	L	NS
Kalahari	-21.00	23.00	500	a	L	NS
Kalahari	-21.00	23.00	1500	a	L	NS
Kalahari	-21.00	23.00	2500	a	L	NS
Kalahari	-21.00	23.00	3500	a	L	NS
Kalahari	-21.00	23.00	5000	a	L	NS
Hatanga	72.00	102.00	500	a	L	NS
Hatanga	72.00	102.00	1500	a	L	NS
Hatanga	72.00	102.00	2500	a	L	NS
Hatanga	72.00	102.00	3500	a	L	NS
Hatanga	72.00	102.00	5000	a	L	NS
LBA-Santarem	-3.00	-55.00	500	a	L	NS
LBA-Santarem	-3.00	-55.00	1000	a	L	NS
LBA-Santarem	-3.00	-55.00	1500	a	L	NS
LBA-Santarem	-3.00	-55.00	2000	a	L	NS
LBA-Santarem	-3.00	-55.00	2500	a	L	NS
LBA-Santarem	-3.00	-55.00	3000	a	L	NS
LBA-Belem	0.00	-47.00	500	a	L	NS
LBA-Belem	0.00	-47.00	1000	a	L	NS
LBA-Belem	0.00	-47.00	1500	a	L	NS
LBA-Belem	0.00	-47.00	2000	a	L	NS
LBA-Belem	0.00	-47.00	2500	a	L	NS
LBA-Belem	0.00	-47.00	3000	a	L	NS
Hypo-Africa	2.00	20.00	500	a	L	NS
Hypo-Africa	2.00	20.00	1500	a	L	NS
Hypo-Africa	2.00	20.00	2500	a	L	NS
Hypo-Africa	2.00	20.00	3500	a	L	NS
Hypo-Africa	2.00	20.00	5000	a	L	NS
Hypo-Africa	2.00	20.00	8000	a	L	NS
Hypo-Africa	2.00	20.00	12000	a	L	NS

3.2 Genetic Algorithms

In a second approach, I used an optimization technique known as a "genetic algorithm" to determine which combination of measurement sites in a given regional or global domain produced the lowest average posterior flux uncertainty from inversions of twelve transport models. I define an "individual", or genome, as a combination of unique CO_2 sampling locations that can possibly be virtual tall tower sites as selected from the existing list of flux towers at which Transcom3 saved high-frequency responses. Each new virtual tall tower is a "gene". Populations of 100 individuals, or virtual tall tower networks, compete to produce the network most robust for reducing carbon flux uncertainty. All networks include the 75 global flask sites and the 4 existing virtual tall tower sites in North America. The genetic algorithm seeks to determine which five or ten additional sites, when combined with the flasks and existing towers, provide the optimal network.

In summary:

gene = virtual tall tower

genome = a unique network of virtual tall towers

population = a group of virtual tall tower networks

In an evolutionary context, the question would be – "Which genome, or unique combination of genes, is most fit to survive and out-compete in this specific environment?" The relevant question in this research context is then – "Which network,

or unique combination of virtual tall towers, is most optimal for producing the greatest flux uncertainty reduction in atmospheric inversions?"

Understanding the technical aspects of this technique can be helpful to recognizing its value as a tool for scientific research. Genetic algorithms (GA) are used in computational optimization schemes in which machine learning can mimic the evolutionary process in nature of natural selection [*Goldberg, 1989*]. Natural systems show remarkable efficiency in self-repair, adaptation, and reproduction, and are a valuable resource after which to model optimization techniques. In an artificial setting, the user controls the environment in which the individual evolves. A measure of fitness is 'robustness', which is understood to be the balance between efficiency and efficacy that is necessary for survival in many different environments. The GA scheme is not a random search for a solution to the problem, where the solution is a highly 'fit' individual. Stochastic processes are incorporated in the algorithm, but the result is distinctly non-random. In the first generation, the algorithm operates on a population of randomly generated individuals, or station lists. In the second and every subsequent generation, the algorithm uses the fitness measure to score a population and thereby improve the next.

The main processing power in genetic algorithms comes from the combination of reproduction according to fitness and crossover. High performing networks are repeatedly tested and exchanged during the search for better performance. There are four main mechanisms that the algorithm uses in its process of optimization: *cross-over,*

mutation, culling, and *refilling*. **Cross-over** probability is the probability that two genomes will be combined. It determines whether the randomly paired genomes remain unchanged or are recombined element by element. The birth of the offspring creates the death of the parents. The children replace the parents and continue the process. Crossover is a structured yet randomized information exchange.

The **mutation** rate is the probability that a specific gene (station) will be changed. Mutation assures that the optimization considers a broad section of the station space, and prevents convergence or a local minimum. Every element for all the lists experiences random variation through the mutation process, so the mutation rate is often very low. For example, a 0.01% mutation rate implies a 0.5 % mutation rate for a 50 station list. The minimum value of the solution is sought, but every possible combination of networks is not considered due to the extensive computational time required to perform such a task. So the solution might turn out to be a local minimum until a mutation is introduced that sets the search domain off course enough to find other non-local minimums. The role of the mutation operator is necessary because the processes of reproduction and cross-over during search and recombination, occasionally lose some potentially useful genetic material, and the mutation operator protects against this loss [*Goldberg, 1989*]. It insures against the premature loss of important information. Mutation rates are small in natural biological populations and therefore we can assume that mutation is a secondary mechanism of adaptation and we assign it to be similarly small. According to *Goldberg* [1989], in order to obtain good results for empirical genetic algorithm studies the frequency of mutation should be prescribed to be on the order of one mutation per

thousand bit (population) transfers. The process of **culling** involves the scoring and ranking of a population. The genome (station list) is then assigned a survival probability based on the resulting reduction of uncertainty in regional fluxes determined by the inversion. Then a random number comparison decides the fate of the genome. The process of **refilling** is necessary after culling. Survivors replace culled members and in this way the best station combinations multiply.

There are other genetic operators and reproductive plans for computational evolution that mimic biology, but these three operators – reproduction, cross-over, and mutation, have been proven to be computationally simple and effective in addressing many optimization problems.

The genetic algorithm used aggregated uncertainty in estimated monthly regional fluxes as a metric to sift through the combinations of stations that create the network which performs best. No station was allowed to be selected more than once for the same network. The metric used was the average root mean square uncertainty for the 12 models, divided by an assumed four or $\sqrt{12}$ degrees of freedom in the seasonal cycle due to temporal autocorrelation for the global and regional experiments, respectively.

For the regional optimization experiment, the following GA metric was used:

$$\frac{\sqrt{sum[(error)^2]/12}}{\sqrt{12}} \tag{5}$$

For the global optimization experiment, the following GA metric was used:

$$\frac{\sqrt{sum[(error)^2]/264}}{4} \tag{6}$$

The "error" in Equations (5) and (6) is constructed from the trace of C_m* (*see section 2.1*), that doesn't include the off-diagonal zero elements of the error covariance matrix. (The "trace" of a matrix is the sum of the squares of the diagonal elements.) A Simple Somewhat Generalized Genetic Algorithm programming code was used for this optimization, as written by *Stefan Kamphausen* [2001]. (*http://www.skamphausen.de/software*) I specified population size and other parameters for these experiments (**Table 4**) based on the number of virtual tall towers eligible to compete, the realistic size of a possible future network, computational efficiency, and discussion of previous GA methods for optimization. [*Peter Rayner, personal communication*].

Table 4. Genetic algorithm parameters.

GA Parameter	Regional Optimization	Global Optimization
Population size	**100**	**100**
Genome length	**5**	**10**
Mutation rate	**0.01**	**0.01**
Cross-over probability	**0.30**	**0.30**
Generations (Iterations)	**100**	**100**

3.3 Experiment 1: Regional Network Optimization

The flask network currently estimates the temperate North America flux uncertainty at ~ 0.4 Gt C yr^{-1}. I investigated how the temperate North American flux uncertainty could be reduced through additions of various combinations of virtual tall towers. Fisrt I tested the sensitivity of the uncertainty reductions in annual mean carbon flux estimates to different levels of representation error. I define "representation error" as representing the expected mismatch between the data and the model due to heterogeneity, unsampled variance of [CO_2], instrument error, etc, or how well the difference between the observational data and the model in the inversion can be minimized.

The map shown in **Figure 7** depicts the locations of towers that were currently operating during the Transcom3 experiment and thus available for this exercise. Since then many more towers have been added to the network and an updated version of this map can be seen on the Ameriflux website, found online at *http://public.ornl.gov/ameriflux/Participants/Sites/index.cfm*.

Existing continuous calibrated [CO_2] measurements are located in Massachusetts, Wisconsin, Texas, Oklahoma, and Saskatchewan, Canada. The site in Texas is a new site and now operational, but data from this tower were not available during the Transcom3 Level 2 experiment and therefore high-frequency timeseries were not saved for that location and made available for the inversions. For this reason, only four of the five

existing [CO_2] measurement locations shown in the map were used in this experiment. All inversions include the 75 flasks.

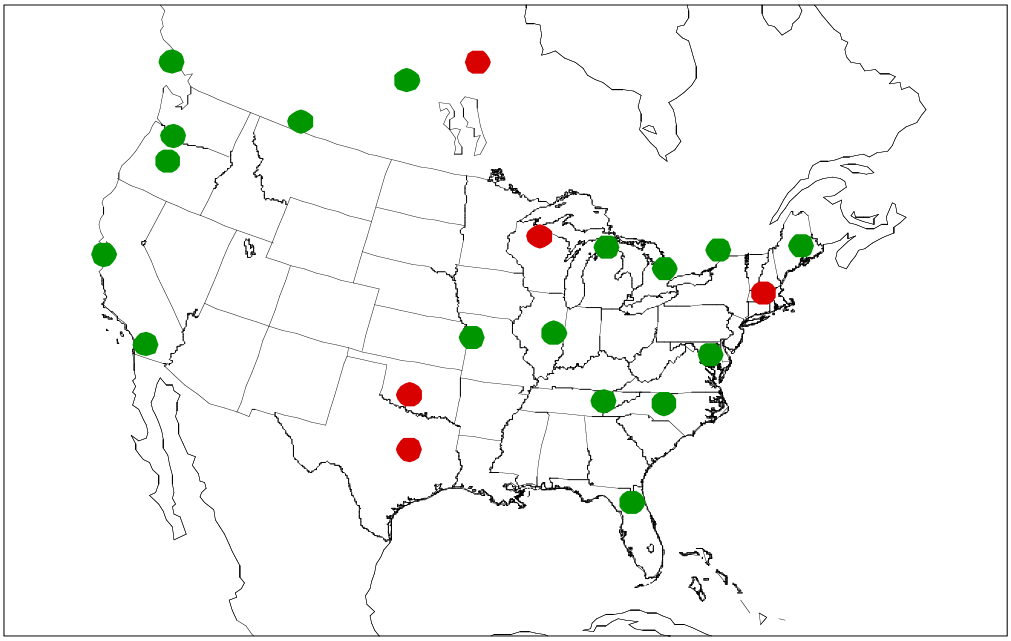

● *Existing* Tower [CO_2] measurements

● *Possible* Tower [CO_2] measurements

Figure 7. Flux tower sites in the Ameriflux network that were eligible for, or already active as, tall tower sites and were saved as high-frequency timeseries from the forward runs of the 12 transport models. (*See Appendix II for site names and locations.*)

A *G matrix* was created for each model for every month and the flux estimate errors generated using the Jacobian matrices from the 12 transport models from the Transcom3 experiment were used. The mean of the variance of the monthly flux estimates for each model was annualized to obtain an overall estimate of model-mean uncertainty in the annual mean flux from each region. First I added four sites to the flask

network that already existed as real tall towers or were being calibrated and therefore already qualified as eligible virtual tall towers. Then I added five new tower sites in addition to the 4 existing towers, and then all 24 of the eligible Ameriflux towers. I tested these networks through inversions of the 12 models from Transcom3 while propagating fifteen different levels of representation error ranging from 0.1 to 20 ppm and ramped to cover different ranges and increments (**Table 5**).

Table 5. Increments of representation error used in the sensitivity experiment.

Level 1 — 0.1 ppm	Level 6 — 1.0 ppm	Level 11 — 5.0 ppm
Level 2 — 0.2 ppm	Level 7 — 1.5 ppm	Level 12 — 7.0 ppm
Level 3 — 0.4 ppm	Level 8 — 2.0 ppm	Level 13 — 10.0 ppm
Level 4 — 0.6 ppm	Level 9 — 2.5 ppm	Level 14 — 15.0 ppm
Level 5 — 0.8 ppm	Level 10 – 3.0 ppm	Level 15 — 20.0 ppm

Then I performed many inversions of five-VTT tower networks that I chose by hand, experimenting with configurations of stations situated in regional clusters, latitudinal bands, coastal transects, and various combinations. (In every case, the experimental grouping of five virtual tall towers was in addition to the flask network and four existing towers.) Inversions using these groups were all performed with a constant representation error lever of 2 ppm. For these calculations the flux uncertainty was defined:

$$\frac{RMS\_error}{\sqrt{4}} \qquad (10)$$

After an initial rudimentary comparison of the uncertainty reductions of about 100 of these hand-picked networks, I then used the genetic algorithm to explicitly determine which network best minimized the uncertainties for the model mean estimates of annualized flux for temperate North America in the inversions. Networks of five towers were allowed to compete in populations of 100 networks according to the parameters described in *Section 3.2*.

3.4 Experiment 2: Global Network Optimization

For the second experiment a global network optimization was performed. As in the regional optimization, the field of global flux tower sites that were considered to be eligible to use as possible virtual tall tower sites came from the high-frequency timeseries saved in Transcom3. **Figure 8** shows the locations of the stations that were used as individual genes for the genetic algorithm. The stations that currently produce calibrated CO_2 concentration data are indicated in purple and correspond to the same sites from the previous regional set-up. Existing stations that are available for the genetic algorithm to use are shown in red. It should be noted that there are many more existing flux tower stations to choose from than are shown in the map. The map indicates that the continents of Africa and most of Asia are devoid of any measurements. Currently, this is not true anymore as several campaigns have established a few observational sites in these areas. However, these continents still remain as some of the most underconstrained areas of the world as well as some of the most problematic for making measurements. They can

benefit the most from a greater density of observations as well as simple implementation strategies.

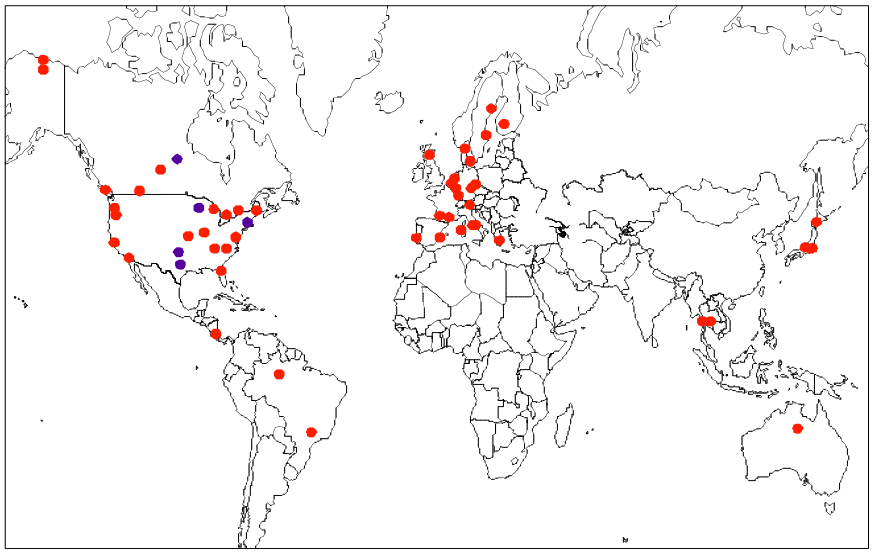

Figure 8. The global network of flux towers considered eligible as virtual tall towers. (*Included are the five existing tall tower sites (purple)).*

The genetic algorithm was initiated with a random population of 100 networks of ten global towers, and operated according to the parameters described in *Section 3.2*. No tower was allowed to be chosen more than once per network, and the populations evolved according to the performance of each configuration in the inversions according to the specified metric. Many iterations were necessary for the solution to converge, e.g. ~80, but once a solution was obtained it remained as a stable solution for more than 1500 iterations.

CHAPTER 4. RESULTS

4.1 Sensitivity of Flux Uncertainty to Representation Error

Significant flux uncertainty reduction resulted from adding 4, 9, and 24 of the Ameriflux towers, acting as virtual tall towers, to the existing flask network. Representation error was gradually decreased from 20 ppm to 0 ppm and a corresponding decrease in flux uncertainty consistently evolved in every case. (**Figure 9.**) A difference from the flux uncertainty of the flask network did not evolve until around 7 ppm for the case with 4 towers, while the 9 tower case and the 24 tower case showed an improvement from the flask network around 10 ppm. The 9 towers reduced uncertainty better than the 4 towers, and the 24 towers reduced uncertainty the most. While all three cases converged to zero uncertainty when zero ppm of representation error was obtained, the reality of the method is not illustrated well in these lower values. Since the error also includes model transport error that cannot be reduced in these methods, near-zero values are probably unachievable.

There is no reduction in the end of the range where representation error is 10 – 20 ppm. This is irrelevant since we already know that we can acquire representation errors of less than 10 ppm. The meaningful information is illustrated at the beginning of the range of 0-10 ppm where uncertainty reductions are obtained on the order of ~25%, ~50%, and ~75% for the 4 tower, 9 tower, and 24 tower additions, respectively.

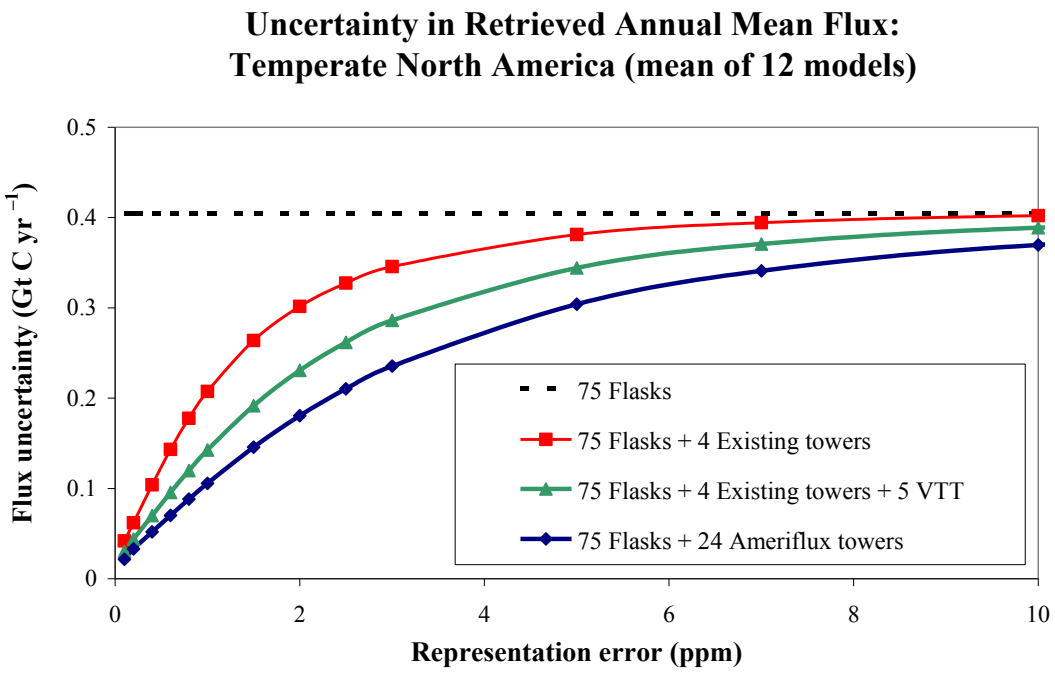

Figure 9. Sensitivity to representation error.

The WLEF analysis showed that a bias much lower than 2 ppm could be achieved – and when 0.2 ppm is considered to be the representation error there is almost a 75% reduction in uncertainty when just five new virtual tall towers are added to the existing network. This indicates that the virtual tall tower methodology has a favorable cost-to-benefit ratio, where the leverage that can be gained in constraining the regional carbon budget from implementing a virtual tall tower network far exceeds the cost of initiating and maintaining such a simple observational network. The flask network expands slowly, but many new flux towers are being funded and established every year. If taking calibrated CO_2 measurements were included in the objectives of all new flux tower campaigns, then five to ten virtual tall towers could be established within the next five years and carbon budget uncertainty in North America would be reduced by 50%.

4.2 Experiment 1: North America Inversions

A comparison of the hand-picked networks shows that some configurations perform better than others in the inversions. An illustration of these differences can be seen in the following figures where different five-tower networks in all of North America are compared (**Figure 10)**, and five-tower networks that are only located in the 30 N to 40 N latitude band of North America (**Figure 11)**. When examples of these groupings and their resulting final uncertainties are compared to each other, the slight but meaningful differences can be seen. (**Table 6.**) Differences range from 0.11 to 0.025 Gt C yr^{-1}. Differences in the latitudinal transect networks are less, ranging from 0.02 to 0.01 Gt C yr^{-1}. The five-tower networks that performed best were clusters of southeastern, midwestern, and mideastern US sites, where vegetation maps show that these regions receive the most precipitation and experience the most biomass growth in the continental US. Southern sites performed better in the inversions than most midwestern sites. Networks consisting of sites only in the western US performed poorly. Ultimately, no purely western, eastern, southern, or northern regional configuration performed better than combinations of sites in several of these areas. Consequently, the same top performing networks chosen here were also selected by the genetic algorithm as the best for reducing North American carbon flux uncertainty. The worst performing networks in this comparison included sites in the western coastal boundaries and the northern Great Lakes region. The genetic algorithm also choose these same configurations for the worst performing networks. These same best and worst networks found in the initial comparison and with the algorithm can be seen in **Figures 12-18**.

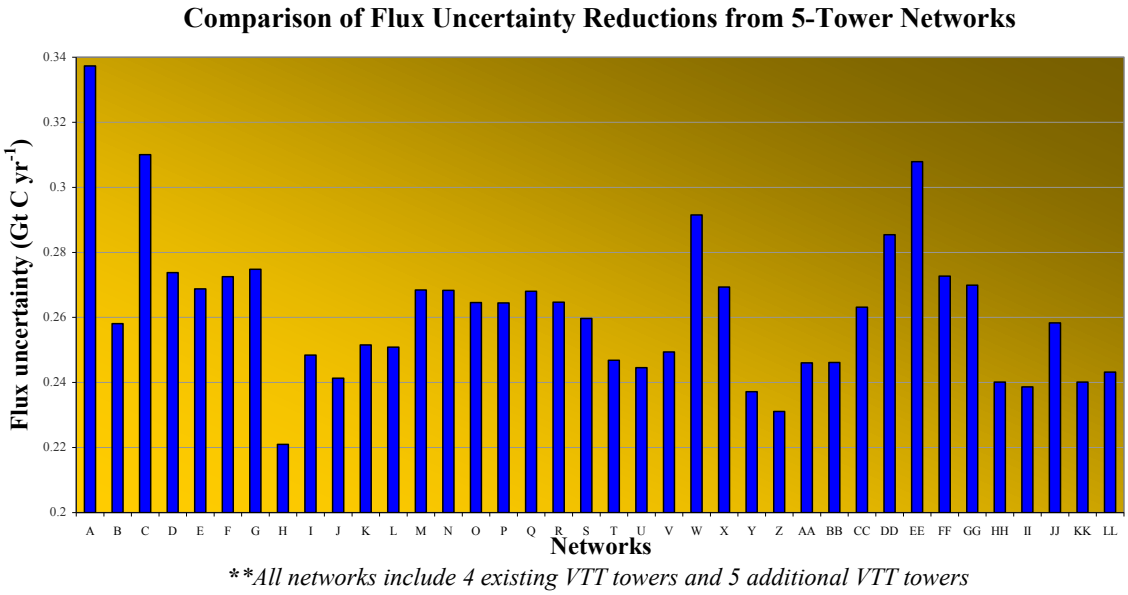

Figure 10. Comparison of flux uncertainty reduction from 5-tower networks.

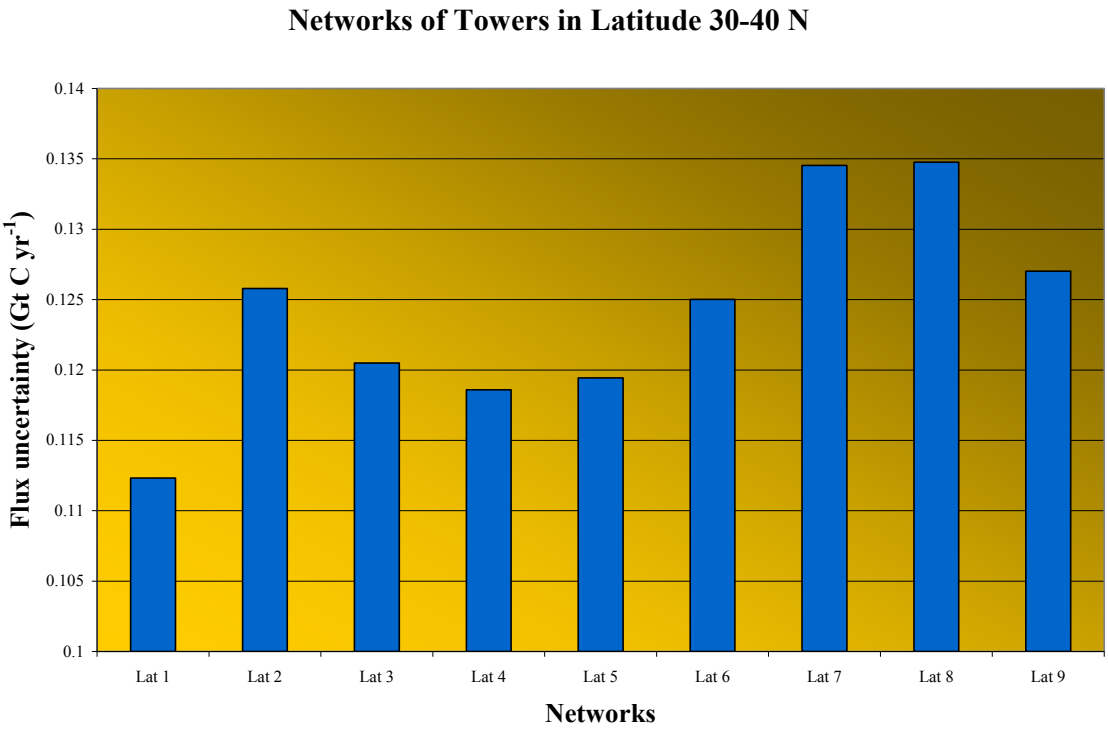

Figure 11. Comparison of flux uncertainty reductions derived from 5-tower combinations all located in the 30 N to 40 N latitude band.

Table 6. Examples of some experimental site groupings and their resulting final uncertainties for the regional North American inversions.

Configuration	Number of Ameriflux towers	Final Uncertainty (Gt C yr^{-1})
Southeast	3	0.31580931
Eastcoast	4	0.30703026
Westcoast	4	0.389798522
Midwest	5	0.29241708
Westcoast + Midwest	9	0.275669038
Westcoast + Eastcoast	8	0.287802636
Westcoast + Southeast	7	0.292353272
Midwest + Southeast	8	0.246241704
Midwest + Eastcoast	9	0.246134832
Southeast + Eastcoast	6	0.2727831
Western US (west of 95 W)	6	0.322831452
Eastern US (east of 95 W)	9	0.244639694
30-40 N Latitude band	8	0.256647378
40-50 N Latitude band	11	0.277762174
50-60 N Latitude band	3	0.42665258

The genetic algorithm produced an optimal network scenario that consisted of five flux tower sites in Illinois, Tennessee, North Carolina, Maryland, and Kansas. (**Figure 12.)** The second-best network produced by the algorithm only differed from the first network by one site. The southeastern Florida site replaced the northeastern Maryland site. (**Figure 13.**) For the third-best network the algorithm changed the Florida site to a site on the west coast of California. (**Figure 14.**) For the fourth-best network the algorithm only maintained the North Carolina site, and moved the other four to a horizontal transect of the Great Lakes to Northeast US region. (**Figure 15.**)

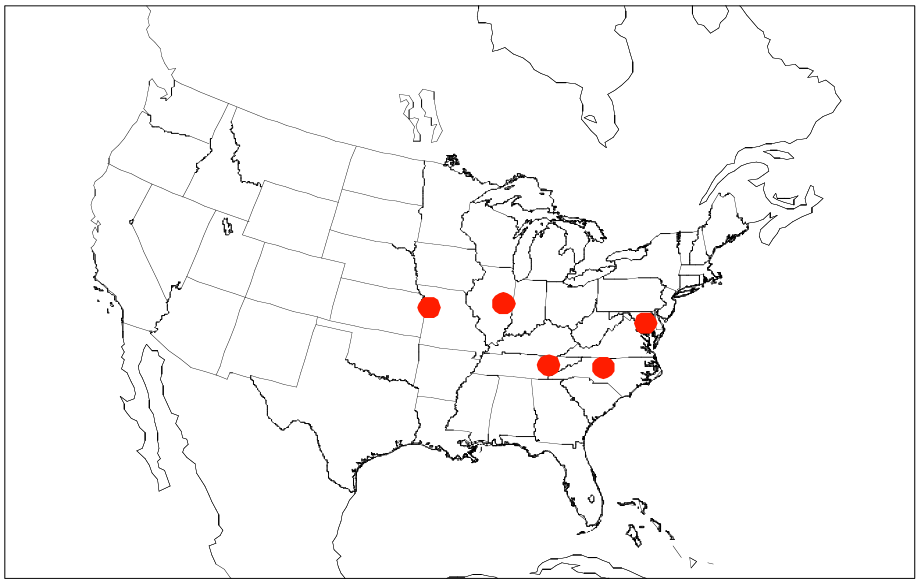

Figure 12. The best performing network derived from the GA optimization scheme.

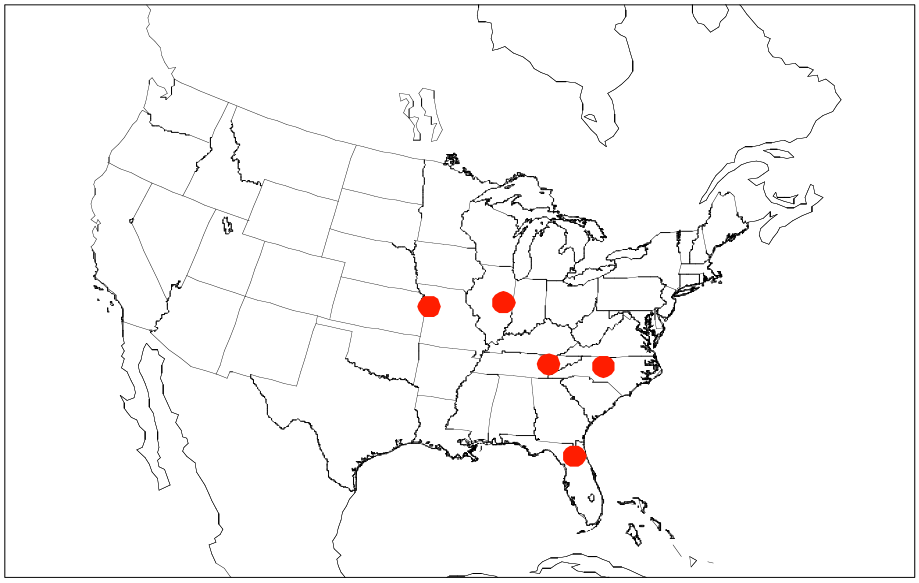

Figure 13. The second – best performing network.

Figure 14. The third – best performing network.

Figure 15. The fourth – best performing network.

In all four optimal networks, the North Carolina site is included and in the top three optimal networks there is consistent selection of the sites in Kansas, Illinois, and Tennessee. The southeast cluster probably works best because it captures the winds as they have already traveled across the North American grid cell and areas of highest biospheric flux in the eastern US.

The network that proved to perform the worst in the inversions consisted of five towers along the western coast. (**Figure 16**.) This particular network represents the strategy of trying to observe an inflow region, or longitudinal transect. It probably performs poorly because it is close to the western boundary of the grid cell and has only received signal from Pacific marine air that has not yet been influenced by the continent. Performing second-worst in the northeast transect with an additional west coast station also doesn't work because it there isn't as much signal coming from the northern forests, plains, and lake regions of southern Canada and northern US.

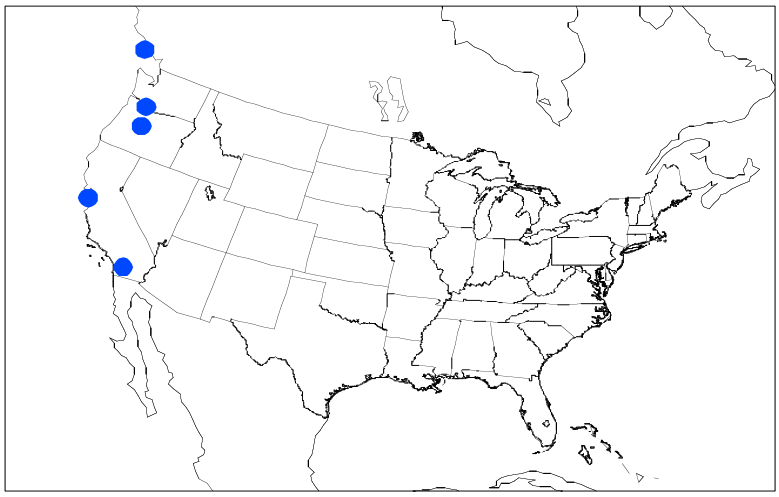

Figure 16. The worst performing network derived from the GA optimization scheme.

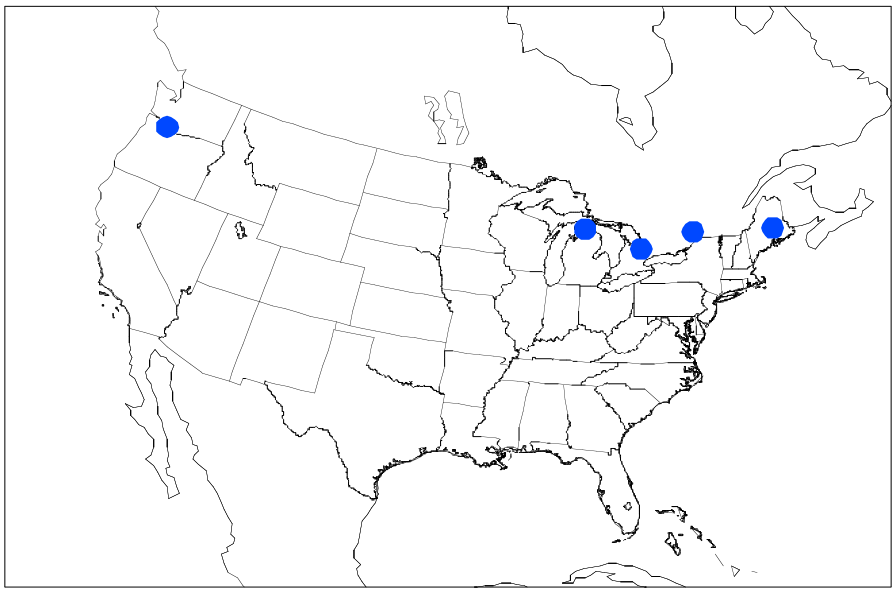

Figure 17. The second – worst performing network.

Figure 18. The third – worst performing network.

In **Figure 19** a comparison is shown between the different types of networks represented by acronyms: FSK represents the flask network only, CNT represents the 4 existing continental sites, CST represents the network where there are only sites on the east and west coasts. TRN represents the sites that line up in a transect across a mid-continental latitude, and CLS represents the combination of sites in the Midwest and Southeastern US. FSK + CNT + CLS also represents the best-performing network from Figure 12. FSK + CNT + CST represents the network presented in Figure 16. FSK + CNT + TRN represents the network presented in Figure 17. The uncertainty reduction between the FSK network (0.4590 Gt C yr^{-1}) and the FSK + CNT + CLS network (0.2311 Gt C yr^{-1}) is equal to 0.228 Gt C yr^{-1}, or equal to a ~ 50% reduction.

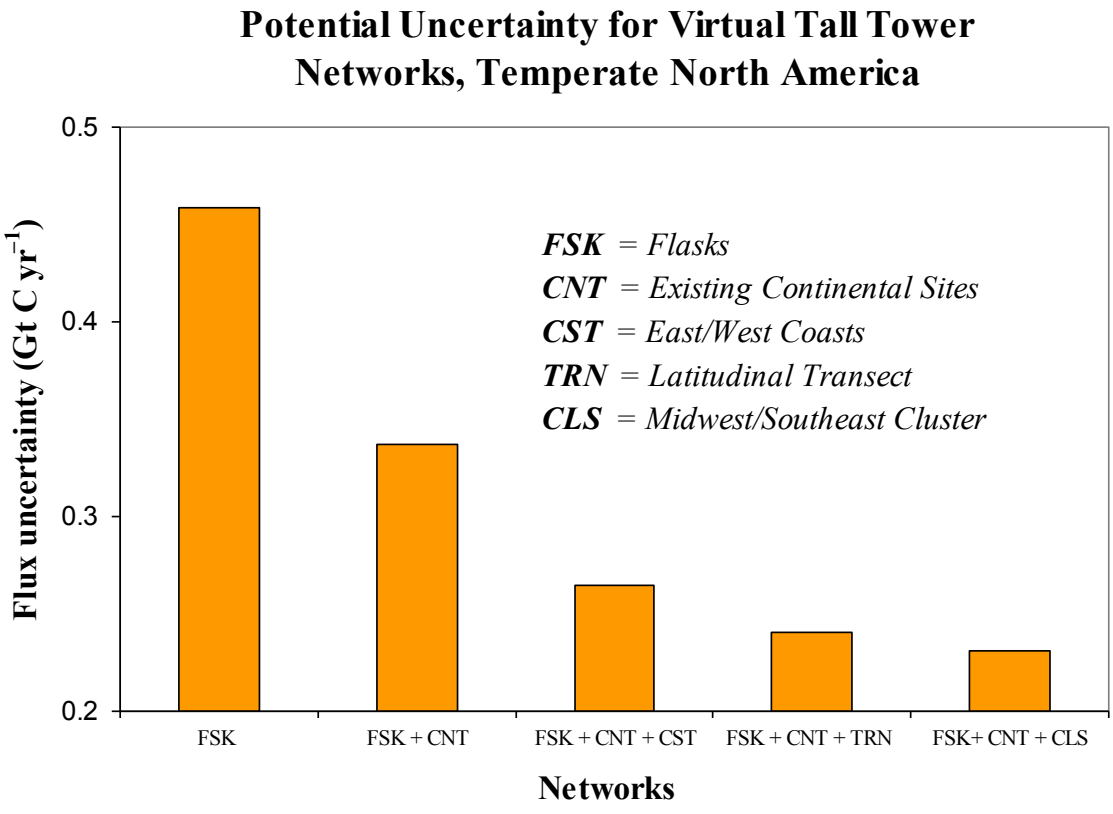

Figure 19. A comparison of uncertainty reductions with different networks.

4.3 Experiment 2: Global Inversions

The genetic algorithm was initialized to compare networks of ten towers in a global domain, while populations of 100 networks were maintained during the evolution. An optimal network converged after 80 iterations, and consistently remained as the optimal solution through 1500 iterations. This network consists of one tower in Spain, one tower in Portugal, two towers in Japan, two towers in Thailand, two towers in Brazil, one tower in Tennessee and one tower in Costa Rica. (**Figure 20.**)

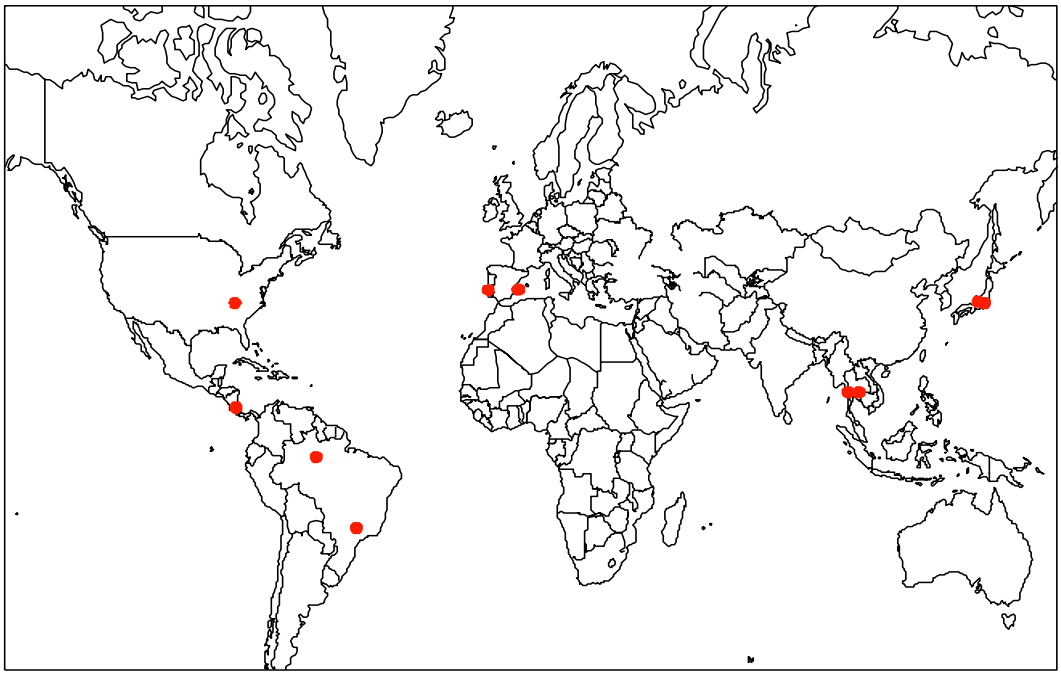

Figure 20. The best performing global network as derived by the optimization scheme.

This scenario is probably optimal because it places towers in the middle of the highest biospheric carbon flux zone in the eastern US and in three locations in tropical America. These areas produce the greatest carbon fluxes in North and South America. There are no stations selected in Africa because there were no high-frequency data time series saved there by Transcom3 for the algorithm to choose. Spain and Portugal were likely both selected – even though Europe is very well constrained, as the best possible way to constrain Africa. Two stations were selected in tropical Asia, and two in Japan. These are likely to better constrain temperate Asia. No towers were chosen from the European network, even though there is a dense population of towers to choose from, because that region is already one of the best constrained regions in the world. (The tower sites in Spain and Portugal are maintained separately from the greater European network, and therefore are identified as being separate.)

The following graph in **Figure 21** shows the flux uncertainty reduction per land and ocean region according to the 22 partitions of Transcom3. The greatest improvement is shown in regions which began the experiment as being the most underconstrained. The greatest improvement is seen in tropical America where the flux uncertainty is reduced by 1.72 Gt C. The second-best improvement is seen in South America with a reduction of 1.45 Gt C. The third-best improvement is seen in tropical Asia where flux uncertainty is reduced by 0.87 Gt C. The highest uncertainties remain in North and South Africa. The least uncertainty reduction occurs in Australia, Europe, Northern Ocean, Southern Ocean, and Indian Ocean. However, these regions remain as the most constrained areas

of the world and are not likely to see improvement in uncertainty reduction before the formerly mentioned regions, regardless of the measurement campaign.

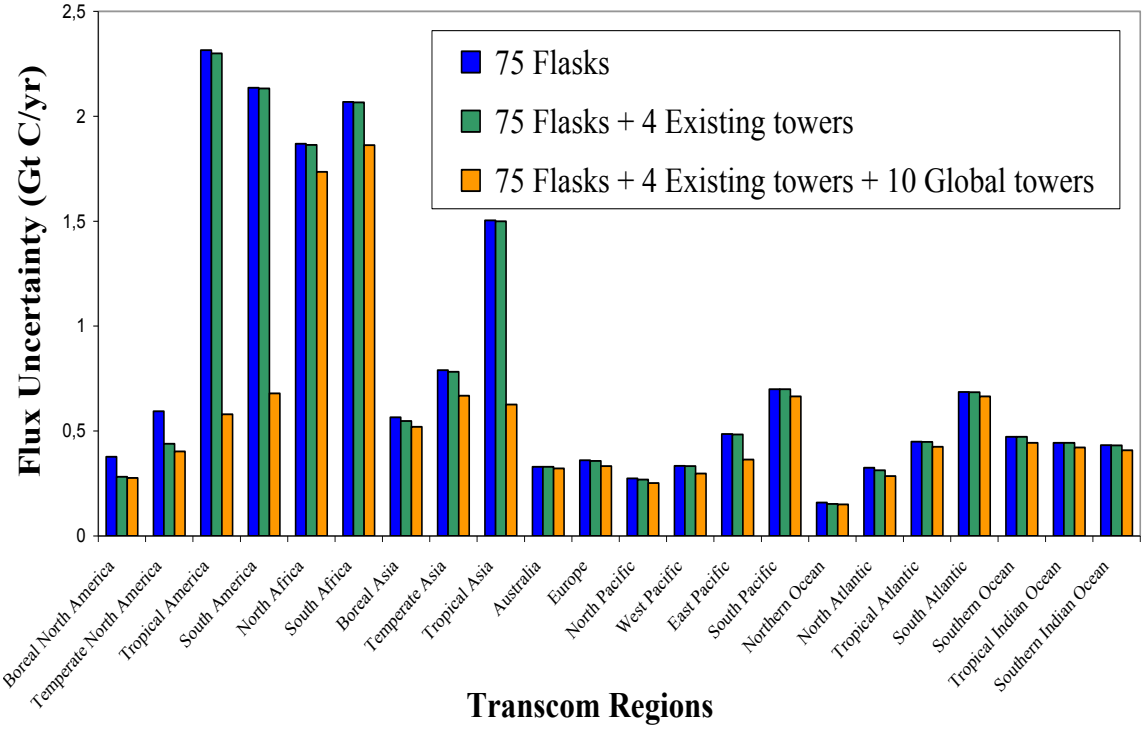

Figure 21. Partitioning of uncertainties between 22 global regions.

Table 8. Uncertainty reduction for the three best performing Transcom regions, assuming a representation error of 2 ppm.

Region	Uncertainty Reduction
Tropical America	1.72 Gt C
South America	1.45 Gt C
Tropical Asia	0.87 Gt C

The European AeroCarb network already has several sites where calibrated [CO_2] measurements are being taken at flux towers, and two real tall towers that already exist. (**Figure 22.)** I performed another global inversion experiment using the assumption that these continuous measurement sites were fixed as virtual tall towers. I also assigned the real tall tower sites to be a fixed part of the existing network, so the genetic algorithm cannot be allowed to build networks by choosing these sites. Being assigned as "fixed" sites, they were thus included in the inversions along with the flask network and the four existing tower sites in North America.

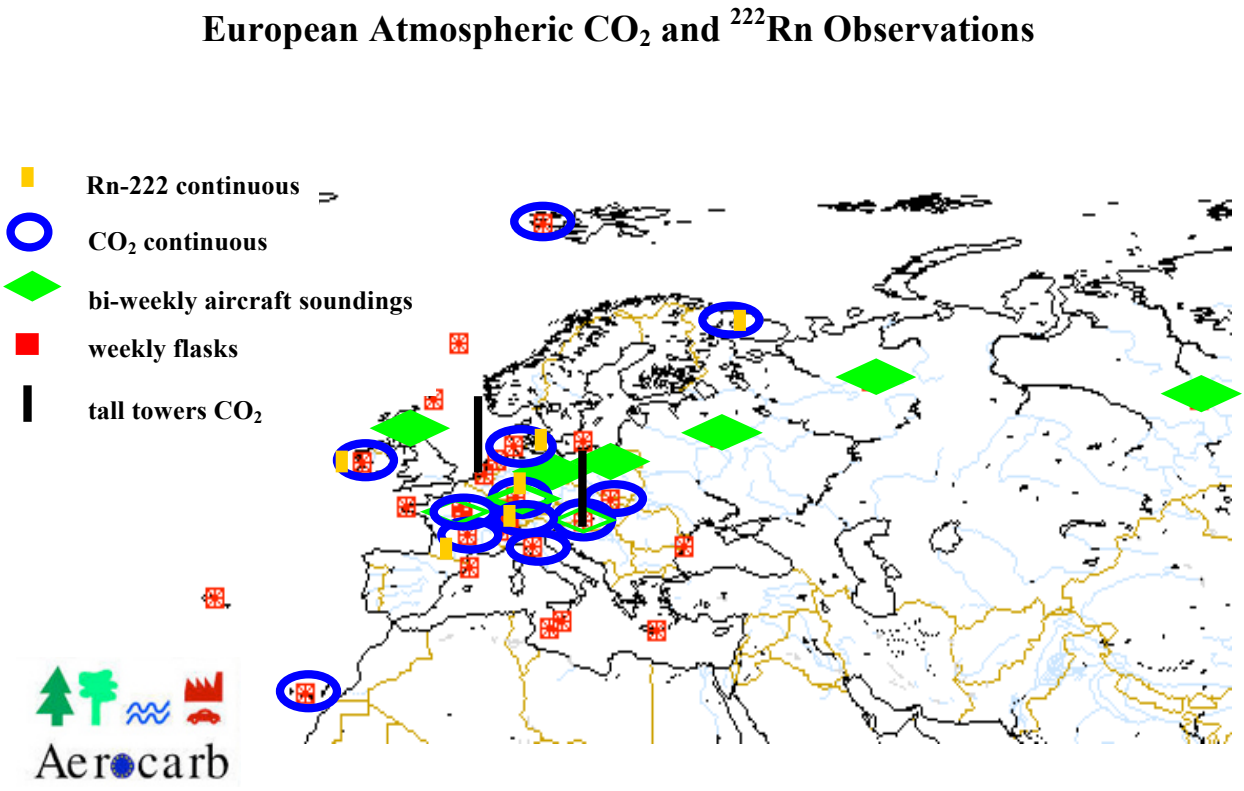

Figure 22. European AeroCarb Network. *Figure courtesy of Phillippe Bousquet.*

When the genetic algorithm was run based on these assumptions, a network was produced that is almost identical to the previous network. There is only one site difference between the two global networks produced. When the inversions assume nothing about the AeroCarb sites, the optimal solution includes a site in Tennessee. When the inversions include the fixed AeroCarb sites, the optimal solution includes a site in Saskatchewan, Canada, in place of the Tennessee site. Spain and Portugal are not part of the AeroCarb network and thus are still available to be chosen, and are indeed chosen again in order to constrain North Africa. The two towers in Thailand and two towers in Japan are also chosen in both experiments, as well as the towers in Brazil and Costa Rica. (**Figure 23.)** These consistent selections indicate that the inversions want to reduce the uncertainties in the large continental regions first as the most efficient way of improving the entire global budget.

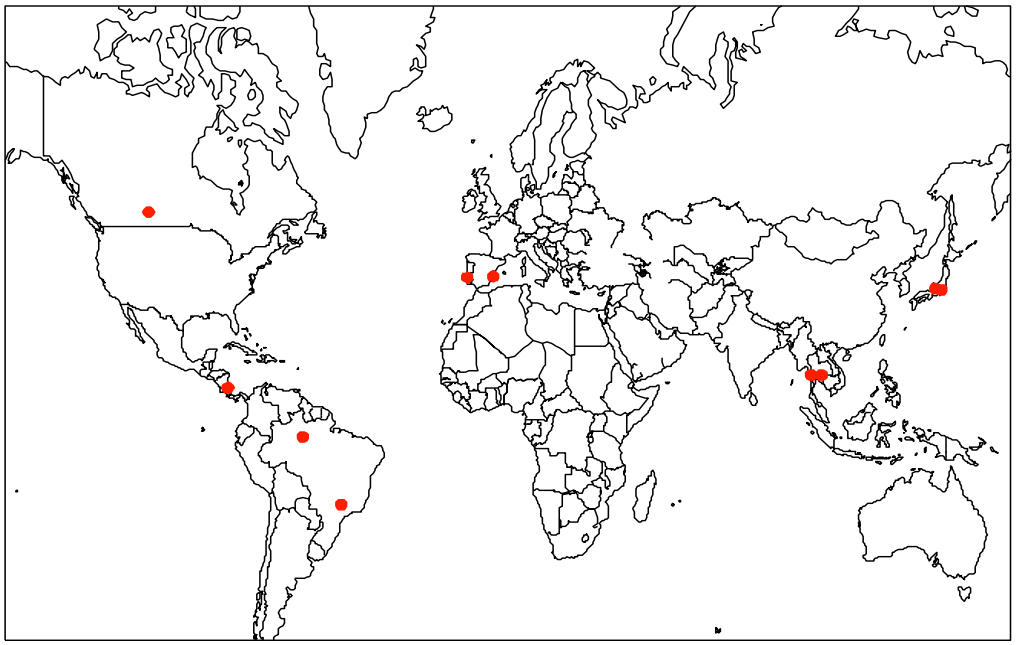

Figure 23. The network selected as most optimal, when AeroCarb towers are included.

CHAPTER 5. CONCLUSIONS

The limited accuracy of regional and global carbon flux estimates due to a paucity of continental measurement stations can be overcome by using a virtual tall tower network. Such a network is created by calibrating CO_2 measurement sensors at existing flux towers, and using data that is already being taken at every site. The results of this study support this idea and provide several conclusions that can help to understand what strategies are best for designing such a network in order to achieve optimal constraint to continental carbon budgets.

Routine continuous calibrated measurements of [CO_2] and other tracers could dramatically improve the uncertainty of regional flux estimates. Creating virtual tall tower networks by combining real tall towers and calibrated measurements at flux towers can provide a dense land observational network that is effective at constraining surface carbon fluxes. Such a network can be established sooner and cheaper than a new real tall tower network. Regional inversions show that a ~50% uncertainty reduction can be achieved in the North American carbon budget by implementing only five new virtual tall towers, when maintained with a 2 ppm representation error. This significant leverage in uncertainty reduction, that can be achieved with minimal cost, shows that virtual tall tower networks are potentially the best value for spending new money on measurement operations.

There are network configuration strategies that work better than others. Optimal virtual tall tower networks emphasize placement *in* and *just downwind* of strong fluxes, not "bracketing" or "gradient" approaches that seek to capture fluxes from both sides or as they change along a latitudinal transect.

High frequency data has more information than monthly means. *Law et al.* [2002] have shown that global inversions can be done using frequent (hourly or daily) measurements. In this way we can take advantage of much bigger signals at synoptic time scales (recall the 35 ppm synoptic variations at WLEF, Sept 1997). This requires accurate transport on regional and synoptic scales. Nonetheless, this strategy is promising for the future because of the results that show dramatic improvement in uncertainty over inversions of monthly mean concentrations.

In the future, it should be investigated as to whether mid-day sampling will produce systematic bias. This can be done by coupling the Colorado State University (CSU) general circulation model with the CSU Simple Biosphere model (SiB) to generate an atmosphere of pseudo-data with diurnally varying fluxes. These pseudo-data can then be inverted using the same cyclostationary inversion code that was used in this study to detect bias that might arise from the mid-day sampling method. The twelve Transcom3 inversion models are central to this particular methodology and it is assumed that the results are congruent with real world scenarios. However, the choice of models might provide bias as well. Ultimately, these simulations of optimal virtual tall tower networks can benefit from validation with other transport models.

REFERENCES

AmeriFlux Site information. Available on-line [http://public.ornl.gov/ameriflux/Participants/Sites/Map/index.cfm] from Oak Ridge National Laboratory Distributed Active Archive Center (ORNL DAAC), Oak Ridge, Tennessee, U.S.A., 2003.

Andres, R. J., G. Marland, I. Fung, and E. Matthews.
A 1° x 1° distribution of carbon dioxide emissions from fossil fuel consumption and cement manufacture, 1950-1990. *Global Biogeochemical Cycles*, **10**, 419-429, 1996.

Bakwin, P. S. and P. P. Tans.
Measurements of carbon dioxide on a very tall tower. *Tellus* **47B**, 535-549, 1995.

Baldocchi, D. D.
Assessing the eddy covariance technique for evaluating carbon dioxide exchange rates of ecosystems: past, present and future. *Global Change Biology*, **9**, 479-492, 2003.

Berger, B. W., K. J. Davis, C. Yi, P. S. Bakwin, and C. L. Zhao.
Long-term carbon dioxide fluxes from a very tall tower in a northern forest: Flux measurement methodology. *Journal of Atmospheric and Oceanic Technology*, **18**, 529-543, 2001.

Brenkert, A. L.
Carbon dioxide emission estimates from fossil fuel burning, hydraulic cement production, and gas flaring for 1995 on a one-degree grid cell basis. [http://cdiac.esd.ornl.gov/ndps/ndp058a.html], 1998.

Bousquet, P., P. Peylin, P. Ciais, C. LeQuere, P. Friedlingstein, and P. Tans.
Regional changes in carbon dioxide fluxes of land and oceans since 1980. *Science*, **290**, 1342-1346, 2000.

Bousquet, P., P. Ciais, P. Peylin, M. Ramonet, and P. Monfray.
Inverse modeling of annual atmospheric CO_2 sources and sinks, 1. Method and control inversion. *Journal of Geophysical Research*, **104**, 26,161-26,178, 1999.

Carbon Dioxide Information Analysis Center (CDIAC)
Available on-line [http://cdiac.esd.ornl.gov/] from Oak Ridge National Laboratory, Oak Ridge, Tennessee, U.S.A., 2003.

Davis, K. J., P. S. Bakwin, C. Yi, B. D. Cook, W. Wang, A. S. Denning, R. M. Teclaw, J. G. Isebrands.
Multiple flux footprints, flux divergences and boundary layer mixing ratios: Studies of ecosystem-atmosphere CO_2 exchange using the WLEF tall tower. Eos. Trans. AGU, **82(20)**, Spring Meet. Suppl., Abstract B41A-03, 2001.

Davis, K. J., S. J. Richardson, P. S. Bakwin, and A. S. Denning.
A virtual tall tower network for understanding continental sources and sinks of CO_2. North American Carbon Program (NACP) Project Description, 1-15, 2003.

Denning, A. S., M. Holzer, K. Gurney, M. Heimann, R. Law, P. Rayner, I. Fung, S. Fan, S. Taguchi, P. Friedlingstein, Y. Balkanski, J. Taylor, M. Maiss, and I. Lavin.
Three-dimensional transport and concentration of SF_6: A model intercomparison study (TransCom2). *Tellus*, **51B**, 266-297, 1999.

Denning, A. S., I. Y. Fung, and D. Randall.
Latitudinal gradient of atmospheric CO_2 due to seasonal exchange with land biota. *Nature*, **376**, 240-243, 1995.

Engelen, R. J., A. S. Denning, K. R. Gurney, and TransCom3 modelers.
On error estimation in atmospheric CO_2 inversions. *Journal of Geophysical Research,* **107(D22)**, 4635-4645, 2002.

Enting, I. G.
Inverse Problems in Atmospheric Constituent Transport, Cambridge Univ. Press, New York, 2002.

Enting, I. G., C. M. Trudinger, and R. J. Francey.
A synthesis inversion of the concentration and $\delta^{13}C$ of atmospheric CO_2. *Tellus*, **47B**, 35-52, 1995.

Fan, S., M. Gloor, J. Mahlman, S. Pacala, J. Sarmiento, T. Takahashi, and P. Tans.
A Large Terrestrial Carbon Sink in North America Implied by Atmospheric and Oceanic Carbon Dioxide Data and Models. *Science*, **282**, 442-446, 1998.

GLOBALVIEW – CO_2: Cooperative Atmospheric Data Integration Project – Carbon Dioxide. CD-ROM, NOAA CMDL, Boulder, Colorado.
[Also available on Internet via anonymous FTP to ftp.cmdl.noaa.gov, Path: ccg/co2/GLOBALVIEW], 2003.

Gloor, M., P. Bakwin, D. Hurst, L. Lock, R. Draxler, and P. Tans.
What is the concentration footprint of a tall tower? *Journal of Geophysical Research*, **106:17**, 831-17840, 2001.

Gloor, M., S. M. Fan, S. Pacala, and J. Sarmiento.
Optimal sampling of the atmosphere for purpose of inverse modeling: A model study. *Global Biogeochemical Cycles*, **14**, 407-428, 2000.

Goldberg, D. E.
Genetic Algorithms in Search, Optimization and Machine Learning. Addison Wesley Longman, Inc., 412 pp., 1989.

Gruber, N., J. L. Sarmiento, and T. F. Stocker.
An improved method for detecting anthropogenic CO_2 in the oceans. *Global Biogeochemical Cycles,* **10**, 809-837, 1996.

Gurney, K. R., R. M. Law, A. S. Denning, P. J. Rayner, D. Baker, P. Bousquest, L. Bruhwiler, Y-H Chen, P. Ciais, S. Fan, I. Y. Fung, M. Gloor, M. Heimann, K. Higuchi, J. John, E. Kowalczyk, T. Maki, S. Maksyutov, P. Peylin, M. Prather, B. C. Pak, B., J. Sarmiento, S. Taguchi, T. Takahashi, and C-W. Yuen.
TransCom3 CO_2 inversion intercomparison: 1. Annual mean control results and sensitivity to transport and prior flux information. *Tellus*, **55B**, 555-579, 2003.

Gurney, K. R., R. M. Law, A. S. Denning, P. J. Rayner, D. Baker, P. Bousquet, L. Bruhwiler, Y-H. Chen, P. Ciais, S. Fan, I. Y. Fung, M. Gloor, M. Heimann, K. Higuchi, J. John, T. Maki, S. Maksyutov, K. Masarie, P. Peylin, M. Prather, B. C. Pak, J. Randerson, J. Sarmiento, S. Taguchi, T. Takahashi, and C-W. Yuen.
Towards robust regional estimates of CO_2 sources and sinks using atmospheric transport models. *Nature*, **415**, 626-630, 2002.

Gurney, K. R., R. Law, P. Rayner, and A. S. Denning.
"TransCom 3 Experimental Protocol," Department of Atmospheric Science, Colorado State University, USA, Paper No. 707, 2000.

Hartmann, D. L.
Global Physical Climatology. Academic Press, 411 pp., 1994.

Houghton, J. T., Y. Ding, D. J. Griggs, M. Noguer, P. J. van der Lindern, and D. Xiaosu.
Climate Change 2001: The Scientific Basis. Contribution of Working Group I to the Third Assessment Report of the Intergovernmental Panel on Climate Change (IPCC). Cambridge University Press, 944 pp, 2001.

Houghton, R. A.
Magnitude, distribution and causes of terrestrial carbon sinks and some implications for policy. *Climate Policy*, **2**, 71-88, 2002.

Houghton, R. A.
The annual net flux of carbon to the atmosphere from changes in land use 1850-1990. *Tellus*, **51B**, 298-313, 1999.

Houghton, R. A., E. A. Davidson, and G. M. Woodwell.
Missing sinks, feedbacks, and understanding the role of terrestrial ecosystems in the global carbon balance. *Global Biogeochemical Cycles*, **12**, 25-34, 1998.

Kaminski, T., P. J. Rayner, M. Heimann, and I. G. Enting.
On aggregation errors in atmospheric transport inversions. *Journal of Geophysical Research*, **106**, 4703-4715, 2001.

Keeling, C. D. and T. P. Whorf.
Atmospheric CO_2 records from sites in the SIO air sampling network. In Trends: A Compendium of Data on Global Change. Carbon Dioxide Information Analysis Center, Oak Ridge National Laboratory, U.S. Department of Energy, Oak Ridge, Tenn., U.S.A., 2003.

Keeling, C. D., R. B. Bacastow, and T. P. Whorf.
Measurements of the concentration of carbon dioxide at Mauna Loa Observatory, Hawaii. In W.C. Clark (ed.), *Carbon Dioxide Review: 1982*. Oxford University Press, New York, 1982.

Law, R. M., Y-H. Chen, K. R. Gurney, and Transcom 3 Modelers.
TransCom 3 CO_2 inversion intercomparison: 2. Sensitivity of annual mean results to data choices. *Tellus*, **55B**, 580-595, 2003.

Law, R. M., P. J. Rayner, L. P. Steele, and I. G. Enting.
Using high temporal frequency data for CO_2 inversions. *Global Biogeochemical Cycles*, **16(4)**, 1053, doi:10.1029/2001GB001593, 2002.

Law, R. M., P. J. Rayner, A. S. Denning, D. Erickson, I. Y. Fung, M. Heimann, S. C. Piper, M. Ramonet, S. Taguchi, J. A. Taylor, C. M. Trudinger, and I. G. Watterson. Variations in modeled atmospheric transport of carbon dioxide and the consequences for CO_2 inversions. *Global Biogeochemical Cycles*, **10**, 783-796, 1996.

Masarie, K. A. and P. P. Tans.
Extension and integration of atmospheric carbon dioxide data into a globally consistent measurement record. *Journal of Geophysical Research*, **100(D6)**, 11,593-11,610, 1995.

Moeng, C.-H.
A large-eddy simulation model for the study of planetary boundary-layer turbulence. *Journal of Atmospheric Science,* **41***,* 2052-2062, 1984.

Patra, P. K., S. Maksyutov, D. Baker, P. Bousquet, L. Bruhwiler, Y-H. Chen, P. Ciais, A. S. Denning, I. Y. Fung, M. Gloor, K. R. Gurney, M. Heimann, K. Higuchi, J. John, R. M. Law, T. Maki, P. Peylin, M. Prather, B. Pak, P. J. Rayner, J. L. Sarmiento, S. Taguchi, T. Takahashi, and C-W. Yuen.
Sensitivity of optimal extension of CO_2 observation networks to model transport. *Tellus*, **55B**, 498-511, 2003.

Patra, P. K., and S. Maksyutov.
Incremental approach to the optimal network design for CO_2 surface source inversion. *Geophysical Research Letters*, **29**, NO. 10, 10.1029/2001GL013943, 2002.

Randerson, J. T., M. V. Thompson, T. J. Conway, I. Y. Fung, and C. B. Field.
The contribution of terrestrial sources and sinks to trends in the seasonal cycle of atmospheric carbon dioxide. *Global Biogechemical Cycles*, **11**, 535-560, 1997.

Raupach, M. R., O. T. Denmead, and F. X. Dunin.
Challenges in linking atmospheric CO_2 concentrations to fluxes at local and regional scales. *Australian Journal of Botany*, **40,** 697-716, 1992.

Rayner, P. J., I. G. Enting, R. J. Francey, and R. Langenfelds.
Reconstructing the recent carbon cycle from atmospheric CO_2, $\delta^{13}CO_2$ and O_2/N_2 observations. *Tellus*, **51B**, 213-232, 1999.

Rayner, P. J., I. G. Enting, and C. M. Trudinger.
Optimizing the CO_2 observing network for constraining sources and sinks. *Tellus*, **48B**, 433-444, 1996.

Rayner, P. J., and R. M. Law.
The interannual variability of the global carbon cycle. *Tellus*, **51B (2)**, 210-212, 1999.

Roedenbeck, C., S. Houweling, M. Gloor, and M. Heimann.
Time-dependent atmospheric CO_2 inversions based on interannually varying tracer transport. *Tellus*, **55B**, 488-497, 2003.

Schimel, D. S.
Terrestrial ecosystems and the carbon cycle. *Global Change Biology*, **1**, 77-91, 1995.

Stull, R. B.
An Introduction to Boundary Layer Meteorology. Kluwer Academic Publishers, 666 pp., 1994.

Tans, P. P.
Why Carbon Dioxide from Fossil Fuel Burning Won't Go Away. *Perspectives in Environmental Chemistry*. Chap. 12, Edited by Donald L. Macalady, Oxford University Press, 1998.

Tans, P. P., I. Y. Fung, and T. Takahashi.
Observational constraints on the global atmospheric carbon dioxide budget. *Science*, **247**, 1431-1438, 1990.

Tans, P. P., T. J. Conway, and T. Nakazawa.
Latitudinal distribution of the sources and sinks of atmospheric carbon dioxide derived from surface observations and atmospheric transport models. *Geophysical Research Letters,* **94**, 5151-5172, 1989.

Tarantola, A.
Inverse Problem Theory. Elsevier Science Pub., The Netherlands, 1987.

Wallace, J. M., and P. V. Hobbs.
Atmospheric Science: An Introductory Survey. Academic Press, 467 pp., 1977.

APPENDICES

Appendix I. Author list for Transcom3 Level 2 Experiment

Kevin Robert Gurney: Department of Atmospheric Science, Colorado State University, Fort Collins, CO, 80523

Rachel M. Law: CSIRO Atmospheric Research, PMB 1, Aspendale, Victoria 3195, Australia

Scott Denning: Department of Atmospheric Science, Colorado State University, Fort Collins, CO, 80523

Peter J. Rayner: CSIRO Atmospheric Research, PMB 1, Aspendale, Victoria 3195, Australia

David Baker: National Center for Atmospheric Research (NCAR), Boulder, CO 80303

Philippe Bousquet: Laboratoire des Sciences du Climat et de l'Environment (LSCE), F-91198 Gif-sur-Yvette Cedex, France

Lori Bruhwiler: National Oceanic and Atmospheric Administration (NOAA), Climate Monitoring and Diagnostics Laboratory, 326 Broadway R/CG1, Boulder, CO 80303

Yu-Han Chen: Department of Earth, Atmospheric, and Planetary Science, Massachussetts Institute of Technology (MIT), Cambridge, MA 02141

Philippe Ciais: Laboratoire des Sciences du Climat et de l'Environment (LSCE), F-91198 Gif-sur-Yvette Cedex, France

Inez Y. Fung: Center for Atmospheric Sciences, McCone Hall, University of California, Berkeley, Berkeley, CA 94720-4767

Martin Heimann: Max-Planck-Institut fur Biogeochemie, D-07701 Jena, Germany

Jasmin John: Center for Atmospheric Sciences, McCone Hall, University of California, Berkeley, Berkeley, CA 94720-4767

Takashi Maki: Quality Assurance Section, Atmospheric Environment Division, Observations Department, Japan Meteorological Agency 1-3-4 Otemachi, Chiyoda-ku, Tokyo 100-8122 Japan

Shamil Maksyutov: Institute for Global Change Research, Frontier Research System for Global Change, Yokohama, 236-0001 Japan

Philippe Peylin: Laboratoire des Sciences du Climat et de l'Environment (LSCE), F-91198 Gif-sur-Yvette Cedex, France

Michael Prather: Earth System Science, University of California, Irvine, CA 92697-3100

Bernard C. Pak: Earth System Science, University of California, Irvine, CA 92697-3100

Shoichi Taguchi: National Institute of Advanced Industrial Science and Technology, 16-1 Onogawa Tsukuba, Ibaraki 305-8569 Japan

Appendix II. The 24 Ameriflux Sites used in this Research

CANADA – Lethbridge, Alberta
CANADA – Mer Bleue, Ontario
CANADA – Campbell River, British Columbia
CANADA – BOREAS NSA, Saskatchewan
CANADA – Camp Borden, Ontario
CANADA – BOREAS SSA, Saskatchewan
COSTA RICA – La Selva
USA – AK Happy Valley, Alaska
USA – AK Upad, Alaska
USA – CA Jasper Ridge, California
USA – CA Sky Oaks Biological Field Station, California
USA – FL Gainesville - cypress wetland, Florida
USA – IL Bondville, Illinois
USA – KS Konza Prairie LTER, Kansas
USA – MA Harvard Forest, Massachusetts
USA – MD Cub Hill (Baltimore), Maryland
USA – ME Howland Forest, Maine
USA – MI University of Michigan Biological Station, Michigan
USA – NC Duke Forest, North Carolina
USA – OK Southern Great Plains ARM site, Lamont, Oklahoma
USA – OR Metolius, Oregon
USA – TN Walker Branch Watershed, Oak Ridge, Tennessee
USA – WA Wind River Crane site, Washington
USA – WI Park Falls/WLEF, Wisconsin

http://public.ornl.gov/ameriflux/Participants/Sites/index.cfm